Article (refereed) – Published version

RESEARCH ARTICLE

Key Points:
- Upper ocean response to typhoon Megi in the northern SCS was examined
- Near inertial response was weak due to nonlinear coupling with diurnal tides
- Surface-layer diurnal energy increased after the passage of Megi

Correspondence to:
J. Tian,
tianjw@ouc.edu.cn

Observed upper ocean response to typhoon Megi (2010) in the Northern South China Sea

Shoude Guan[1], Wei Zhao[1], John Huthnance[2], Jiwei Tian[1], and Jinhu Wang[1]

[1]Key Laboratory of Physical Oceanography, Ocean University of China, Qingdao, China, [2]National Oceanography Center, Liverpool, UK

Abstract Typhoon Megi passed between two subsurface moorings in the northern South China Sea in October 2010 and the upper ocean thermal and dynamical response with strong internal tides present was examined in detail. The entire observed water column (60–360 m) was cooled due to strong Ekman-pumped upwelling (up to 50 m in the thermocline) by Megi, with maximum cooling of 4.2°C occurring in thermocline. A relatively weak (maximum amplitude of 0.4 m s^{-1}) and quickly damped (*e*-folding time scale of 2 inertial periods) near-inertial oscillation (NIO) was observed in the mixed layer. Power spectrum and wavelet analyses both indicated an energy peak appearing at exactly the sum frequency $fD1$ (with maximum amplitude up to 0.2 m s^{-1}) of NIO (f) and diurnal tide ($D1$), indicating enhanced nonlinear wave-wave interaction between f and $D1$ during and after typhoon. Numerical experiments suggested that energy transfer from NIO to $fD1$ via nonlinear interaction between f and $D1$ may have limited the growth and accelerated the damping of mixed layer NIO generated by Megi. The occurrence of $fD1$ had a high correlation with NIO; the vertical nonlinear momentum term, associated with the vertical shear of NIO and vertical velocity of $D1$ or vertical shear of $D1$ and vertical velocity of NIO, was more than 10 times larger than the horizontal terms and was responsible for forcing $fD1$. After Megi, surface-layer diurnal energy was enhanced by up to 100%, attributed to the combined effect of the increased surface-layer stratification and additional Megi-forced diurnal current.

1. Introduction

Tropical cyclones (TCs) represent one of the most intense atmospheric events passing over the tropical and subtropical oceans. Against the background of global warming, it is reported that the frequency and intensity of TCs are increasing over the past 30 years (e.g., occurrence of super typhoon Haiyan, probably the most intense TC recorded, hitting the Philippines in November 2013) [*Emanuel*, 2005; *Chan and Shi*, 1996]. Thus, accurate forecasting of TC track and intensity, as well as accurate predictions of storm surges and ocean waves, are becoming even more important to reduce the threats to lives and property induced by TCs in coastal regions. To improve the forecasting and prediction, a better understanding of the physics of the extreme air-sea interaction under a TC system is required.

Generally, strong near-inertial oscillations (NIOs) can be generated in the upper ocean mixed layer (ML) by moving TCs [*Price*, 1983; *Qi et al.*, 1995; *Shay et al.*, 1998], and persist for many days in the ML before decay, which is thought to be mainly due to the downward propagation into the thermocline and even the deep ocean as near-inertial internal wave packets [*Gill*, 1984; *D'Asaro*, 1989; *Garrett*, 2001]. The observed amplitude of NIOs in the ML was up to 1.6 m s^{-1} under category 3 TC Frances (2004) in the Atlantic Ocean [*Sanford et al.*, 2007, 2011]. An even stronger current response (>2 m s^{-1}) was reported by *Teague et al.* [2007] in the shelf and slope region of the Gulf of Mexico when hurricane Ivan (2004) passed directly over a predeployed mooring array (consisting of 14 moorings). Given the strong vertical shear of the near-inertial currents, intense turbulent mixing via shear instability often follows a TC and entrains colder upper thermocline water into the ML, resulting in significant ML cooling, in addition to the cooling by Ekman-pumped upwelling and upward heat flux at the air-sea interface [*Price*, 1981]. Along tracks of TCs, significant Sea Surface Temperature (SST) cooling by about 1–6°C is usually observed and generally dominated by the vertical entrainment [*Price*, 1981; *D'Asaro et al.*, 2007]. Furthermore, the SST cooling may reduce or even shut down heat fluxes from the ocean to the atmosphere, significantly affecting the evolution and intensity fluctuations of TCs, i.e., a negative feedback of the ocean [*Chang and Anthes*, 1978]. Therefore, in extreme

TC conditions, the roles of the underlying ocean and the upper ocean response in formation and maintenance of TCs have always been interesting topics and have been focused on in recent studies [*D'Asaro et al.*, 2007; *Lin et al.*, 2009].

Over the past 30 years, observations and model experiments both indicated that the background ocean environment, such as mesoscale eddies, ocean fronts and so on, could significantly modulate the upper ocean dynamical and thermal response to a TC [*Jaimes and Shay*, 2009, 2010]. *Jaimes and Shay* [2009] showed that, for similar wind forces under hurricanes Katrina and Rita, the ML velocity response was nearly twice as large inside the cold core eddies as it was in warm core eddies depending on the preTC ocean ML thickness topography. Due to the stronger near-inertial current response and shallower thermocline, more intense ML cooling was often observed inside cold core eddies than warm core eddies. *Chiang et al.* [2011] reported an unusually intense SST cooling, about 10.8°C, dominated by upwelling because of the combined effect of the slow TC translation speed and especially the shallow thermocline due to the presence of a cold eddy. Warm core eddies are more favorable for the near-inertial internal waves to propagate downward to the subsurface as in a "chimney," as demonstrated by *Oey et al.* [2008]. Then an interesting stalling (at approximately 640 m depth) phenomenon was observed in their work when the near-inertial waves were surrounded by strong positive vorticity. Therefore, upper ocean response is significantly related to the preexisting background ocean features.

The South China Sea (SCS) is the largest marginal sea of the western north Pacific and on average about 10.2 typhoons per year traverse the SCS (from the western north Pacific or generated locally) [*Wang et al.*, 2007]. Due to the special geographic location and complex topography, many scales of motion are active in the SCS, including large-scale circulation [*Su*, 2004], mesoscale eddies [*Wang et al.*, 2003; *Zhang et al.*, 2013], and particularly the strong internal tides [*Alford et al.*, 2010; *Xu et al.*, 2012]. At Luzon Strait, strong diurnal and semidiurnal internal tides are generated when the barotropic tide flows over seamounts, and then propagate away into the SCS [*Niwa and Hibiya*, 2004; *Jan et al.*, 2007]. Via the active nonlinear wave-wave interactions among the near-inertial internal waves, diurnal and semidiurnal tides [*Alford*, 2008; *Xie et al.*, 2008, 2011], these internal tidal energy finally dissipates in the SCS and contributes to the enhanced diapycnal mixing in the deep SCS [*Tian et al.*, 2009].

Therefore, the complex background ocean environment in the SCS may confer a complicated modulation on the upper ocean response to typhoons; especially, the strong internal tides, which have been hardly discussed in previous studies, may particularly affect the internal wave wake. Despite much previous work on the upper ocean response to typhoons in the SCS, numerical model simulations are mostly used, and direct observations under typhoon conditions are very sparse in the SCS so far. A few studies based on observations from moorings were reported recently, but their mooring locations were too far away from the typhoon tracks [*Chen et al.*, 2010] or on the continental shelf [*Sun et al.*, 2011]. *Chen et al.* [2013] examined the seasonal variation of NIOs in the SCS and its relation with typhoons and eddies, but neither response to a specific typhoon nor the potential effect of internal tides was discussed.

In October 2010, typhoon Megi passed by a mooring array in the northern SCS, deployed during the South China Sea Internal Wave Experiment (SCSIWEX). This occurrence provided a rare opportunity to examine the upper ocean response to a typhoon, based on the continuous current and temperature profiles measured by the mooring array, as well as the nonlinear wave-wave interactions between typhoon-induced near-inertial internal waves and the diurnal internal tide. This work aims to examine the upper ocean thermal and dynamical response to typhoon Megi with the presence of strong internal tides. Typhoon Megi and the observational experiment are introduced in section 2; an overview of the thermal and dynamical response is presented in section 3; the NIOs response is examined in section 4; the mechanism for nonlinear wave-wave interaction between NIOs and diurnal internal tides is analyzed in section 5; section 6 focuses on the burst of diurnal energy after Megi; discussion and conclusions are presented in section 7.

2. Typhoon Megi, Data, and Methods

2.1. Typhoon Megi

Typhoon Megi, a category 5 tropical cyclone on the Saffir-Simpson hurricane scale, was the most intense typhoon recorded worldwide in 2010 and in the western north Pacific in the last 20 years (until super typhoon Haiyan in 2013). The track of typhoon Megi is shown in Figure 1. The intensity and best-track data
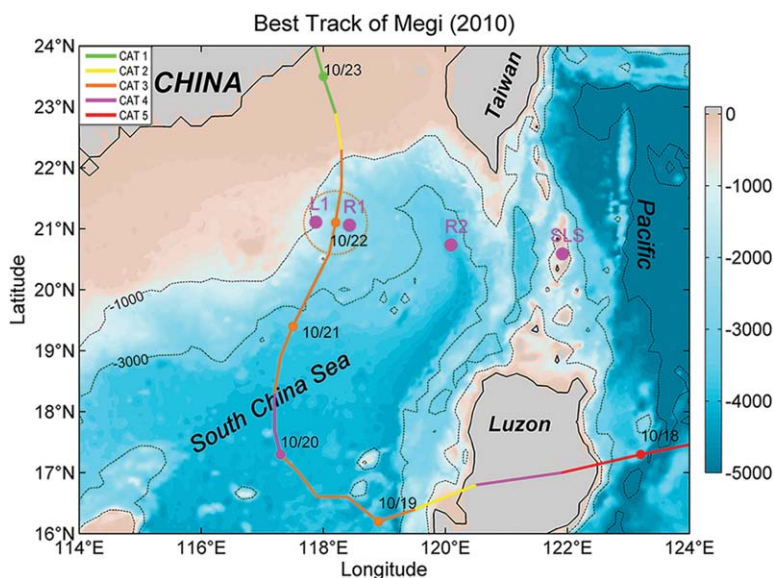
Figure 1. Best track (curve) of typhoon Megi (2010) and topography of the SCS (color). Different colors of the curve and points stand for different intensities according to the Saffir-Simpson scale. Magenta dots represent the positions of subsurface moorings (L1, R1, and R2). The magenta dot SLS at Luzon Strait is selected to represent the source of internal tides as in *Ramp et al.* [2010]. The maximum wind radius of Megi at 0000 UTC on 22 October is indicated by the dashed brown circle. The 1000 and 3000 m isobaths are shown as black contours.

of typhoon Megi used in this study were obtained from Joint Typhoon Warning Center (JTWC; available online at http://www.usno.navy.mil/JTWC). The best-track data include the location of the TC center, as well as the intensity (maximum sustained winds in knots) and radius of the maximum wind every 6 h. Developed as a tropical depression in the western north Pacific, Megi intensified gradually as it proceeded on a westerly course and reached category 5 on 17 October east of the Philippines. At 1800 UTC on 18 October, typhoon Megi passed through the Philippines into the SCS, and then dropped to category 2. Typhoon Megi then quickly reintensified to category 4 at 1800 UTC on 19 October and headed to the northern SCS. Megi lingered in the SCS for 5 days with relatively slow speed of 2.0–3.5 m s^{-1} and made landfall on the southern coast of Fujian on 23 October. At 0000 UTC on 22 October, the center of typhoon Megi passed through a mooring array deployed by the Ocean University of China and the main analysis in this paper is based on the data sets from the mooring array (Figure 1).

2.2. Subsurface Mooring Array

As part of the South China Sea Internal Wave Experiment (SCSIWEX), three moorings (L1, R1, and R2, from west to east) were deployed in the northern SCS (Figure 1) from August 2010 to April 2011. The water depths at the three mooring positions of L1, R1, and R2 were 968, 2480, and 3745 m, respectively. The center of typhoon Megi, as a category-3 intensity TC, passed between moorings L1 and R1 at 0000 UTC on 22 October, with a relatively slow translation speed of 2.8 m s^{-1} and maximum sustained wind speed of 56 m s^{-1}. The radius of the maximum wind speed was 55 km, as shown in Figure 1. Mooring L1 was about 30 km to the left, whereas moorings R1 and R2 were approximately 25 and 200 km to the right of the typhoon track. Moorings L1 and R1 were inside the maximum wind speed circle; a stronger response was observed at both of these moorings than at R2 and will be focused on in this study.

The moorings were equipped with 75 kHz Acoustic Doppler Current Profilers (ADCPs) at a depth approximately 400 to 500 m, as well as temperature chains, to measure the upper ocean velocity, temperature, and salinity. Moorings L1, R1, and R2 were each equipped with an upward-looking 75 kHz ADCP to measure the velocity from near the instrument to the ML (Table 1 and Figure 3). All of the ADCPs sampled the upper ocean in 8 m bins and formed ensembles every 3 or 5 min. Mooring R1 was equipped with a 300 m long temperature chain, that covered 60 to 360 m depth, and consisted of 2 Seabird 37SM CTDs and 28 thermometers to monitor the temperature and salinity variations in the upper layers. The sampling time interval of the temperature-chain was 1 min, with 10 m vertical resolution. Detailed information about each mooring is shown in Table 1.

Table 1. Moorings Deployed in the Northern SCS

Mooring	Observation Period	Longitude, Latitude	Water Depth (m)	Instruments	Instrument Depth (m)	Range Depth (m)	Sample Interval (min)	Bin Size (m)
L1	23 Aug 2010 to 20 Apr 2011	117°52.66′E, 21°06.57′N	968	Upward-looking 75 kHz ADCP	436	35–425	3	8
R1	25 Aug 2010 to 20 Apr 2011	118°25.61′E, 21°03.59′N	2480	CTD	60		1	
				T-chain	**a	70–150	1	10
				CTD	160		1	
				T-chain	**	170–360	1	10
				Upward-looking 75 kHz ADCP	370	50–360	3	8
R2	12 Apr 2010 to 20 Apr 2011	120°05.50′E, 20°44.15′N	3745	Upward-looking 75 kHz ADCP	465	50–450	5	8

[a]There are nine thermometers here, so the depth of each one is not indicated for simplicity.

Under the influence of strong background currents associated with internal waves or mesoscale eddies, the moorings occasionally had large vertical excursions. Given that the real-time depth information of the instruments is recorded by the two CTDs and ADCPs, all the velocity and temperature data were interpolated onto uniform levels at 5 m intervals. In addition, all velocity and temperature data were averaged every 30 min to produce time series with 30 min resolution. After preprocessing, the effective vertical ranges of velocity were 35–420 m, 50–375 m, and 50–490 m for moorings L1, R1, and R2, respectively (Table 1 and Figure 3). Based on a fixed 300 m length, the temperature-chain moves up and down, strongly affected by the background current, and the effective vertical range of temperature measured at mooring R1 was approximately 60–360 m (Figure 2a) with gaps appearing at the top or lower layers.

2.3. Slab Model

A simple mixed-layer slab model developed by *Pollard and Millard* [1970] was used to simulate the NIOs in the ML generated by typhoon Megi. For mixed-layer depth H, over which the wind stress is assumed to be
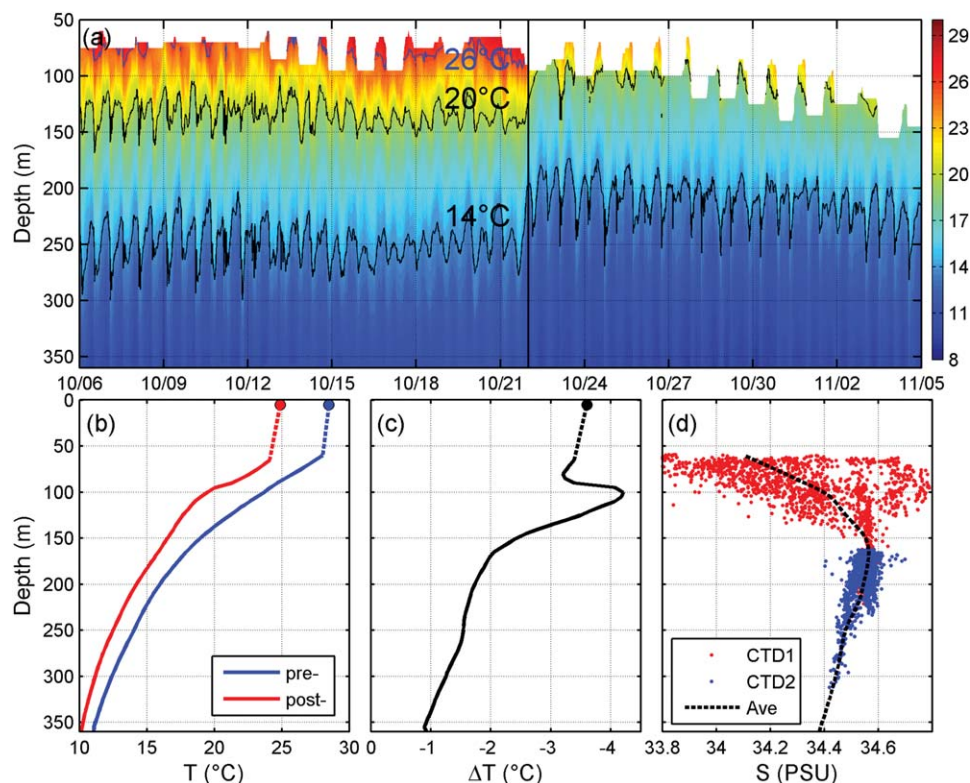
Figure 2. (Top, a) contour plot (color) of temperature (°C) versus depth and time for mooring R1. The 14, 20, and 26°C isothermal lines are plotted and labeled; the 26°C isothermal line is blue. (Bottom, b) average temperature profiles before (blue) and after (red) typhoon Megi. SST and the uppermost temperature from temperature-chain are linked by dashed lines due to insufficient measurements. This simplification hardly affects the result. (c) Temperature drop calculated from profiles in Figure 2b. (d) Scatter of salinity measured by the two moored CTDs in October. The dashed line is the average at each depth.

distributed as a body force, the equations for eastward (u) and northward (v) components of ML velocity are as follows:

$$\frac{\partial u}{\partial t} - fv = \frac{\tau_x}{\rho H} - ru, \tag{1}$$

$$\frac{\partial v}{\partial t} + fu = \frac{\tau_y}{\rho H} - rv, \tag{2}$$

where τ_x and τ_y are the surface wind stress components, f is the local inertial frequency, ρ is the density of seawater, and r is an empirical damping coefficient parameterizing the decay of ML near-inertial currents, resulting from the lateral and downward propagation of near-inertial internal waves, energy loss to mixing via shear instability, or other physical processes that may result in the loss of ML near-inertial energy.

The slab model has been widely used and validated for producing realistic simulations of the near-inertial current response to impulsive wind events [*Pollard and Millard*, 1970; *Pollard*, 1980; *D'Asaro*, 1985; *Alford*, 2001].

2.4. 3DPWP Model

Considering the simplicity of the slab model with only a linear damping term and no near-inertial internal wave wake, a three-dimensional version of the numerical Price-Weller-Pinkel model (3DPWP) [*Price et al.*, 1986] developed by *Price et al.* [1994], was also used to simulate the upper ocean response to typhoon Megi. The 3DPWP model was widely used and performed fairly well in simulating upper ocean response to tropical cyclones [*Sanford et al.*, 2007, 2011].

The 3DPWP model solves the momentum, heat, and salt budget equations on a fixed grid; the only subgrid-scale process is the shear-driven vertical mixing parameterized by the one-dimensional ocean model of *Price et al.* [1986]. The grid interval is 10 m vertically and is uniform down to 150 m where it expands and continues to 450 m with a 20 m vertical interval. The horizontal resolution is 9 km and uniform.

2.5. CFSR Reanalysis Wind Field

Given the lack of field observed wind fields of typhoon Megi, the wind stress fields used in this work to drive the slab and 3DPWP model were the fine spatial and temporal resolution (hourly and $0.3° \times 0.3°$) data sets from the NCEP Climate Forecasting System Reanalysis (CFSR) selected hourly time series products [*Saha et al.*, 2010; available online at http://rda.ucar.edu/datasets/ds093.1]. The CFSR winds successfully captured the track and structure of typhoon Megi but failed to capture its intensity with the maximal wind speed of about 38 m s^{-1} on 22 October, which is less than the estimate from the JTWC of 56 m s^{-1}. Compared with the intensity estimates from JTWC with limited data sets, the CFSR products generally underestimated the wind speed of Megi by a factor of approximately 1.2–1.5 from 19 to 23 October. For simplicity, the wind speed of CFSR was artificially increased by a factor of 1.4 in order to drive the slab and 3DPWP model using a more realistic wind field.

Recent studies suggested that the commonly used drag coefficient C_d [e.g., *Large and Pond*, 1981] that increases linearly with wind speed (usually 10 m height wind speed, U_{10}) is not valid at high wind speeds [*Powell et al.*, 2003; *Jarosz et al.*, 2007], and an overestimation of the energy input into the upper ocean is often obtained when modeling the oceanic response to TCs [*Sanford et al.*, 2007]. Thus, the present study adopted the formula proposed by *Oey et al.* [2006], which fits the *Large and Pond* [1981] formula at low-to-moderate wind speeds and *Powell et al.* [2003] at high wind speeds (equation (3)).

$$
\begin{aligned}
C_d \times 1000 &= 1.2, & U_{10} &< 11 \ m/s \\
&= 0.49 + 0.065 U_{10}, & 11 &< U_{10} \le 19 \ m/s \\
&= 1.364 + 0.0234 U_{10} - 0.00023158 & U_{10}^2 \quad 19 &< U_{10} \le 100 \ m/s
\end{aligned}
\tag{3}
$$

The wind stress field $\vec{\tau}$ was calculated via equation (4):

$$\vec{\tau} = \rho_a C_d U_{10} \vec{u}_{10}, \tag{4}$$

where ρ_a is the air density and $\vec{u}_{10}$ is the wind velocity vector. The estimated wind stress at moorings L1 and R1 is shown in Figures 9a and 9b.

3. Upper Ocean Thermal and Dynamical Response

3.1. Thermal Response

The R1 temperature profiles and the satellite-observed SST from Merged MicroWave and InfraRed SST daily products (MW_IR SST) were combined to analyze the upper ocean thermal response to typhoon Megi. MW_IR SST data are produced by Remote Sensing Systems and sponsored by the National Oceanographic Partnership Program (NOPP), the NASA Earth Science Physical Oceanography Program, and the NASA MEaS-UREs DISCOVER Project. Data are available at www.remss.com. Figure 2a shows the upper ocean thermal structure evolving at mooring R1; the time-averaged temperature profiles at depth and SST before (16–21 October) and after (22–25 October) typhoon Megi are shown in Figure 2b.

The pretyphoon oceanographic conditions had a thick warm layer, with the TC-critical 26°C isotherm line at about 80 m depth (Figure 2a). Before typhoon Megi, the averaged SST was 28.50°C and the temperature observed by the temperature-chains at the top layer (60 m) was 28.05°C, so the pretyphoon ML depth was estimated to be about 60 m, based on a ML definition that the temperature at the ML base was lower by 0.5°C than SST, as in *Watanabe and Hibiya* [2002]. After the passage of typhoon Megi, the SST decreased to 24.9°C, so the SST was cooled by about 3.6°C under typhoon Megi.

For cases with ML cooling dominated by vertical entrainment, as usually observed and demonstrated in previous studies [e.g., *Price*, 1981], colder thermocline water is entrained up to cool the ML; moreover, the warmer ML water is entrained down, and warming at the ML base and upper thermocline is commonly measured. However, a rapid rise of isotherms up to 50 m toward the sea surface was observed over nearly the entire observed water column (from 60 to 360 m; Figure 2a), indicating a strong Ekman-pumped upwelling due to the subcritically slow translation speed and thus long duration of typhoon Megi in this region (similar to the Kai-Tak case presented by *Chiang et al.* [2011], where upwelling dominated the SST cooling). The entire observed water column was cooled under typhoon Megi and the maximum cooling was 4.2°C, occurring in the thermocline at 100 m depth (more intense cooling than in the ML; Figures 2b and 2c). Based on the pre and posttyphoon time-averaged temperature profiles in Figure 2b, the upper ocean heat content (OHC) from the sea surface to 360 m was estimated via equation (5):

$$OHC = \rho_0 C_p \int_{360}^{0} T(z)dz, \tag{5}$$

where $\rho_0 = 1024$ kg m^{-3} is the reference water density, and $C_p = 4000$ J Kg^{-1}°C^{-1} is the heat capacity. Under the influence of typhoon Megi, the estimated ocean heat content (equation (5), referred to 0°C) decreased by 13%, from 554 J cm^{-2} before Megi to 484 J cm^{-2} after Megi.

The ML depth was shallower after Megi but could not be estimated accurately, because the temperature difference between the surface and the top of the temperature-chain (65 m) was up to 0.9°C, with no measurement between them. After typhoon Megi had passed, the upper layers slowly warmed and the isotherms returned to pretyphoon levels about 20 days later.

3.2. Overview of Current Response

The eye (center) of typhoon Megi crossed the line between moorings L1 and R1 at 0000 UTC on 22 October, with the peak wind speed of about 56 m s^{-1}. Before typhoon Megi, the background current was fairly strong (up to 0.7–0.9 m s^{-1}; Figure 3), including signals from large-scale circulation, mesoscale eddies, and particularly the strong internal tides, etc. When typhoon Megi passed by, significant energy was injected into the upper ocean, and the raw current velocity increased immediately at both moorings L1 and R1. The maximum current speed at both moorings increased to 1.2–1.5 m s^{-1}. Figure 3 shows that the velocity increase was more obvious above the 100 m depth. However, compared with the large surface layer current increase observed under hurricane Frances in the North Atlantic [e.g., *Sanford et al.*, 2007, 2011] (up to 1.6 m s^{-1}) or
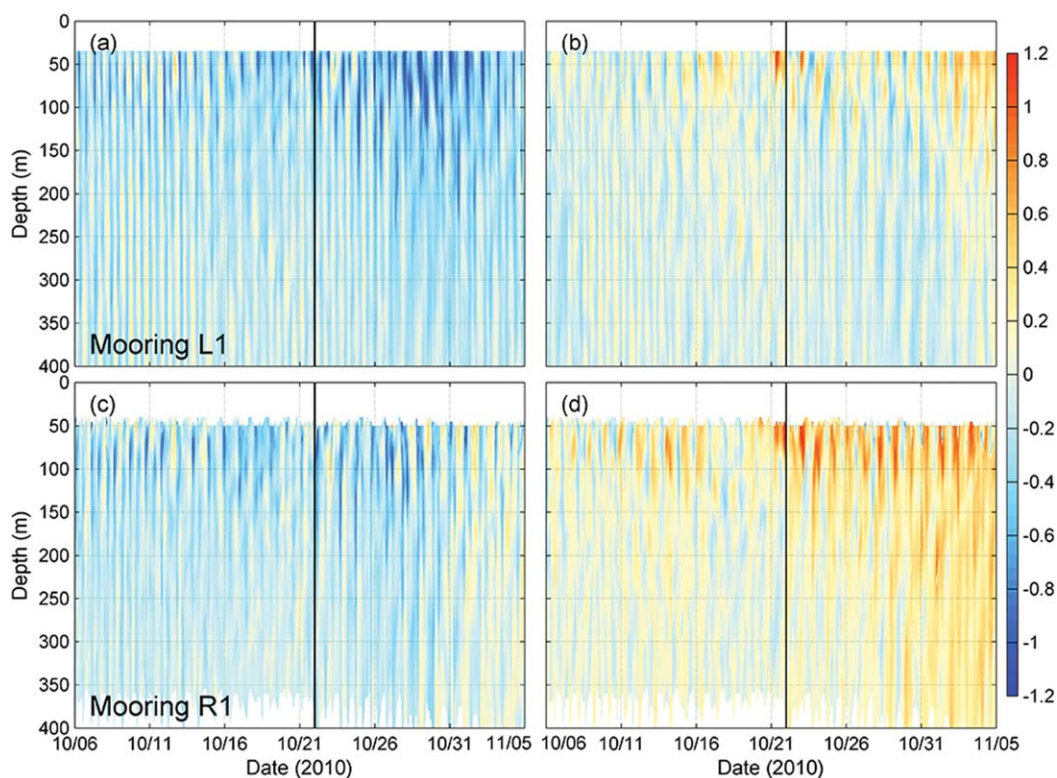
Figure 3. Contours of (left) eastward and (right) northward components of the raw current velocity versus time and depth for (a, b) moorings L1 and (c, d) R1. Vertical line represents the time when typhoon Megi passed.

under hurricane Ivan in the northern Gulf of Mexico [e.g., *Teague et al.*, 2007] (>2 m s^{-1}), the current increase of approximately 0.5–0.7 m s^{-1} under typhoon Megi was fairly small. Moreover, *Teague et al.* [2007] measured a strong current response (>1 m s^{-1}) below 150 m depth; however, under typhoon Megi a much weaker current increase (<0.3 m s^{-1}) was observed.

The typhoon-generated near-inertial currents interfered with the internal tidal current and were masked in the strong background flow (Figure 3). The depth-averaged v component velocity spectra above 100 m (35–100 m for L1 and 50–100 m for R1) for pre and posttyphoon conditions were calculated for moorings L1 (Figure 4a) and R1 (Figure 4b) by means of the smoothed periodogram spectral method [*Bloomfield*, 2000]. Velocity spectra of u components were similar to those of v components and are not shown here. After the passage of typhoon Megi, the near-inertial energy increased by up to 5–10 times compared with the pretyphoon condition. Unlike previous observational results with a predominant near-inertial oscillation, the internal tides, particularly the diurnal tide (*D1*), still dominated the internal wave band in the upper layers after Megi as they did before. Hereafter, *Di* (*i* = 1, 2, 3, etc.) is used to represent an (over) harmonic of the diurnal band if no specific harmonic frequency is indicated. It is notable that a new spectral peak at the sum frequency (denoted as *fD1* hereafter) of inertial (*f*) and diurnal (*D1*) frequencies appeared after typhoon Megi, and the energy at *fD1* frequency increased by up to 10 times at both moorings L1 and R1. Considering there is no external force just at the *fD1* frequency, this suggests that a triad nonlinear wave-wave interaction may occur among the typhoon-generated near-inertial internal wave, the diurnal internal tide and a third wave *fD1* at their sum frequency. Moreover, the surface-layer diurnal energy also increased significantly after the passage of Megi.

To further examine the current response at each frequency, the currents near inertial, diurnal and *fD1* frequencies were extracted by means of a fourth-order Butterworth filter applied in the time domain. The filter was applied twice, once forward and once backward to minimize the phase distortion. The upper and lower limits for the filter are (0.80, 1.13)*f* (0.58–0.81 cpd at mooring R1) for the near-inertial oscillations, (0.86, 1.09)
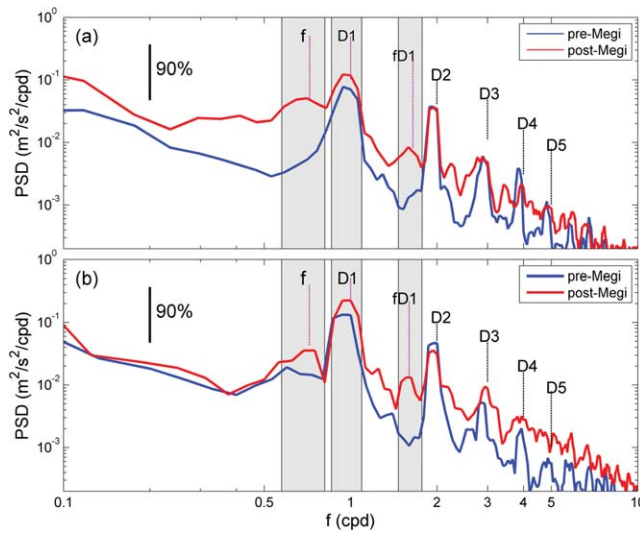
Figure 4. Depth-averaged power spectra (top layer to 100 m) of the v-component veloc-ity before (6–21 October) and after (22 October to 05 November) typhoon Megi for moor-ings (a) L1 and (b) R1. The f, $D1$, $fD1$ and major harmonic frequencies are indicated. The 90% statistical significance level is indicated by the vertical bar near the upper left corner. The frequency bands of f, $D1$, and $fD1$ for the band-pass filtering are shaded.

$K1$ (0.86–1.09 cpd) for diurnal tides and (0.85, 1.03) ($f + K1$) (1.47–1.77 cpd at mooring R1) for $fD1$. The bandwidths (shaded areas in Figure 4) for each fre-quency were chosen wide enough to maximally extract the currents of the three bands, while narrow enough to remove energy from adjacent frequen-cies (e.g., $D1$; f and $fD1$; $D2$).

3.3. Near-Inertial Oscillations
At midday on 20 October, typhoon Megi began to influence moorings L1 and R1 and acceler-ated the near-inertial oscillations in the ML (Figure 5). At both moorings L1 and R1, the ampli-tudes of NIOs in the mixed layer gradually increased to a maxi-mum value of about 0.4 m s^{-1} on 22 October, much smaller than

that observed under hurricane Frances with the same storm intensity [*Sanford et al.*, 2007] (the amplitude was up to 1.6 m s^{-1}). After the passage of Megi, the amplitude of NIOs decreased quickly with an *e*-folding decay time scale of about 2 inertial periods (33.4 h at L1 and 33.3 h at R1), much quicker damping than in other observations [*Teague et al.*, 2007; *Qi et al.*, 1995] (persisting more than 10 days after storms). Thus, a
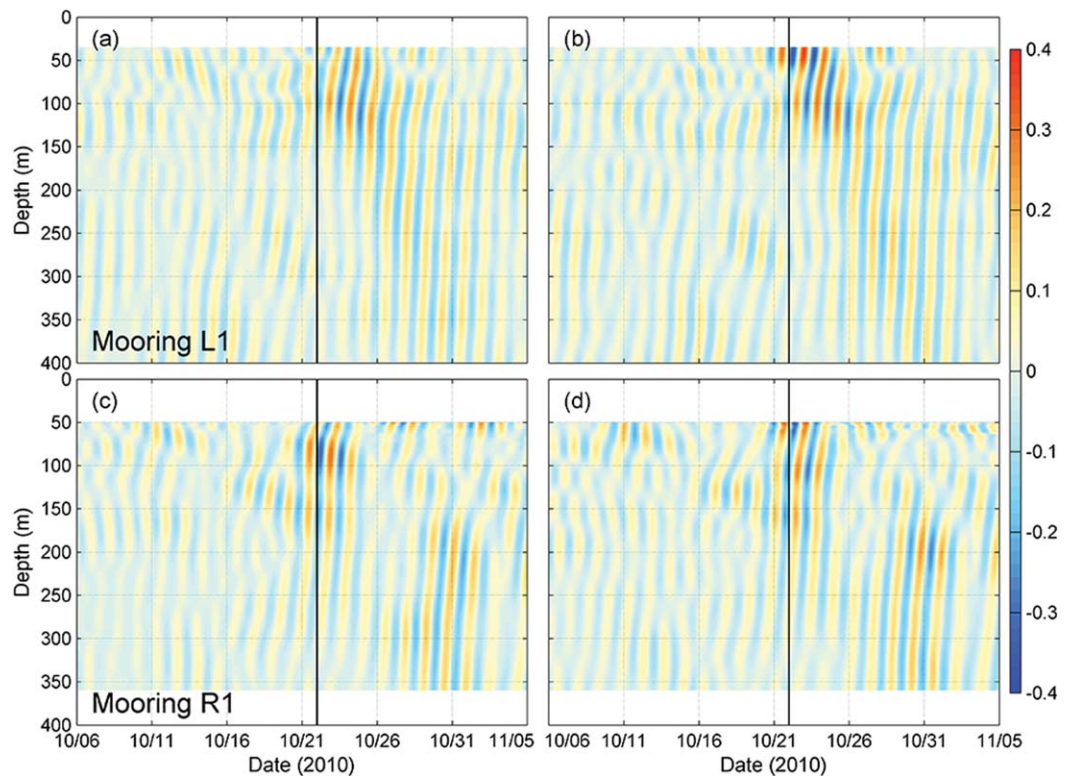
Figure 5. Contours of (left) eastward and (right) northward components of the near-inertial current (m s^{-1}) versus time and depth for (a, b) moorings L1 and (c, d) R1. The vertical line represents the time when typhoon Megi passed.
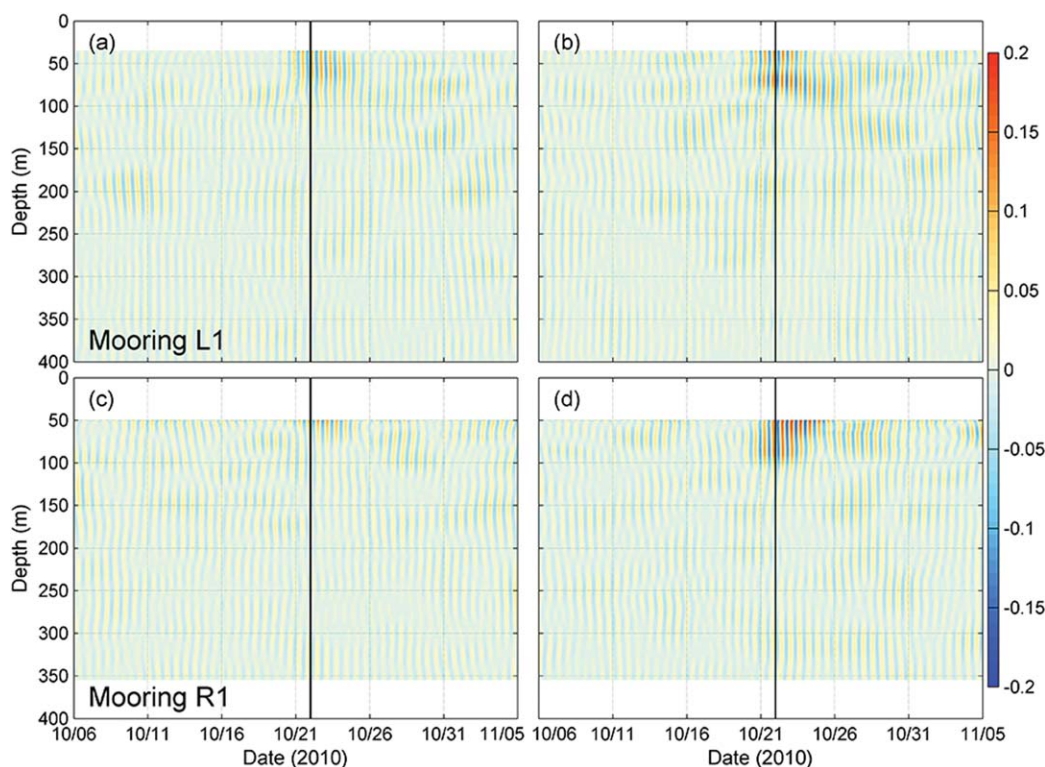
Figure 6. Similar to Figure 5, but for *fD1*.

relatively weak and more quickly damped ML NIO was observed under typhoon Megi in the northern SCS. The damping of NIOs was commonly attributed to the lateral and downward radiation of near-inertial waves and local dissipation. In the present work, damping of NIOs is further related to its nonlinear coupling with diurnal tide and this will be demonstrated in detail via model experiments in section 4.

The near-inertial current had an upward propagating phase, so the vertical component of group velocity was downward, indicating that the near-inertial energy propagated downward into the thermocline as near-inertial internal waves, as is apparent in Figure 5. From 26 to 29 October, the NIO in the ML increased again, resulting from strong winds related to the subsequent typhoon Chaba passing east of Luzon Strait.

3.4. fD1 Current

Following the enhancement of NIO, the amplitude of *fD1* currents increased significantly (from less than 0.05 m s^{-1}) at both moorings during and after the passage of typhoon Megi (Figure 6). The maximum amplitudes of *fD1* currents were 0.17 m s^{-1} and 0.23 m s^{-1} at moorings L1 and R1, respectively, nearly half of the amplitude of NIO. In the presence of strong diurnal internal tides in the SCS, the mooring motion may also produce a *fD1* signal when near-inertial current flows over the mooring cable. Thus, the mooring motions were first examined using ADCP measured depth and temperature data. However, no energy peak was found at *fD1* frequency. The vertical excursions of the ADCPs at *fD1* frequency were small (mostly less than 5 m) with a maximum potential horizontal velocity less than 1 cm s^{-1}. This is far too small to affect our measurements. Therefore, the measured *fD1* current should be a part of the ocean response to typhoon Megi, not a false signal from mooring motions. As with the NIOs, the northward *fD1* component was larger than the eastward component, particularly at mooring R1. It is notable that the enhancement of *fD1* was confined to the upper 100 m, and its growth and decay were highly correlated with that of NIOs, implying the crucial role of NIOs in generating the third wave *fD1* via nonlinear wave-wave interaction. The mechanism of the nonlinear interaction among NIOs, diurnal tide and *fD1* will be discussed in detail in section 5.
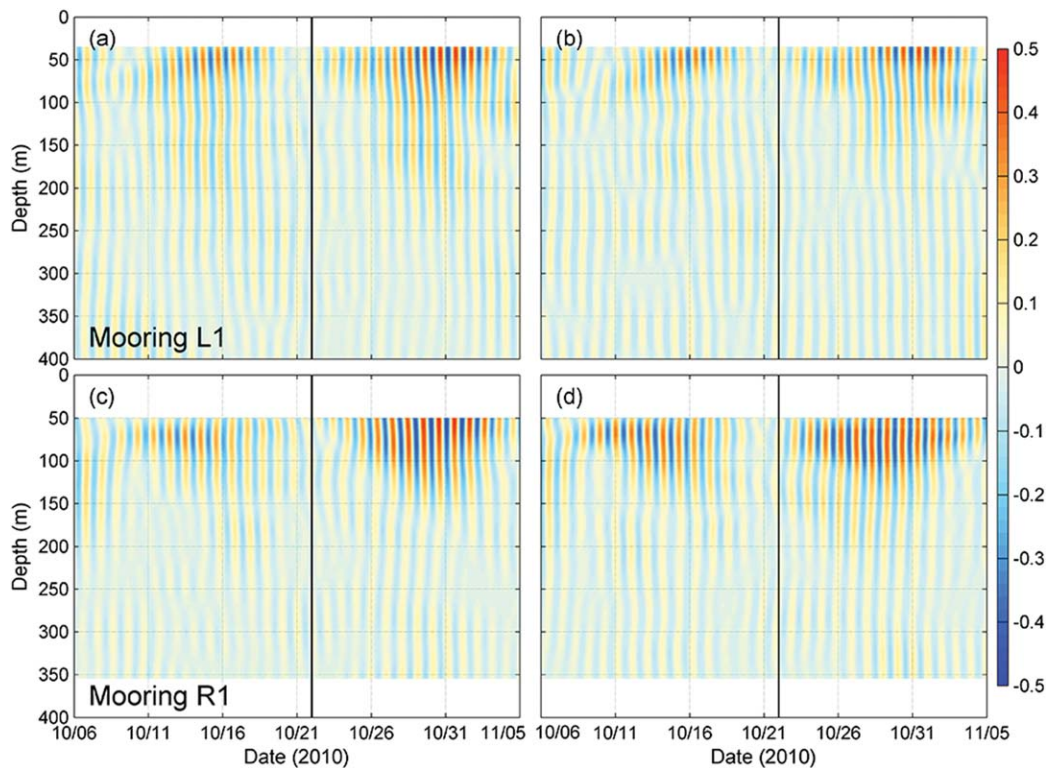
Figure 7. Similar to Figure 5, but for the diurnal tide.

3.5. Diurnal Current

Previous studies demonstrated that K1 and O1 harmonics dominate the diurnal tide in the SCS [e.g., *Xu et al.*, 2012]. Therefore, the filtered diurnal current presents a fortnightly spring-neap tidal cycle (Figure 7). Although we only have partial vertical coverage (the water depth was larger than the measurement range that we obtained), the diurnal barotropic tide predicted from TPXO7.2 inverse model [*Egbert and Erofeeva*, 2002] at moorings L1 and R1 was 10 times smaller than the filtered diurnal current, so the filtered current was assumed to be a mostly baroclinic diurnal tide.

Typhoon Megi passed through the moorings at neap tides (Figure 7). Spectral analysis indicated a surface-layer diurnal current increase post-Megi. Compared with the spring tide on 14–17 October (pre-Megi), the spring tide post-Megi was significantly enhanced on 29 October to 1 November, particularly in the upper 100 m. The current speed was increased by up to 10 cm s^{-1} at both moorings. The increase of the surface-layer diurnal currents and their relation with typhoon Megi will be discussed in detail in section 6.

4. Relatively Weak and Quickly Damped NIOs Under Typhoon Megi

4.1. Quickly Damped Near-Inertial Kinetic Energy

Based on the filtered near-inertial current, the near-inertial kinetic energy density E_f was estimated via equation (6):

$$E_f = \frac{1}{2}\rho_0(u_f^2 + v_f^2),$$

(6)

where $\rho_0 = 1024$ kg m^{-3} is the reference water density, u_f and v_f are the filtered eastward and northward components of near-inertial current.

To examine the life of surface-layer near-inertial kinetic energy generated by typhoon Megi, E_f was further period-smoothed ($\sim$34 h smoothed), and then depth-averaged above 100 m (shown in Figure 8a for
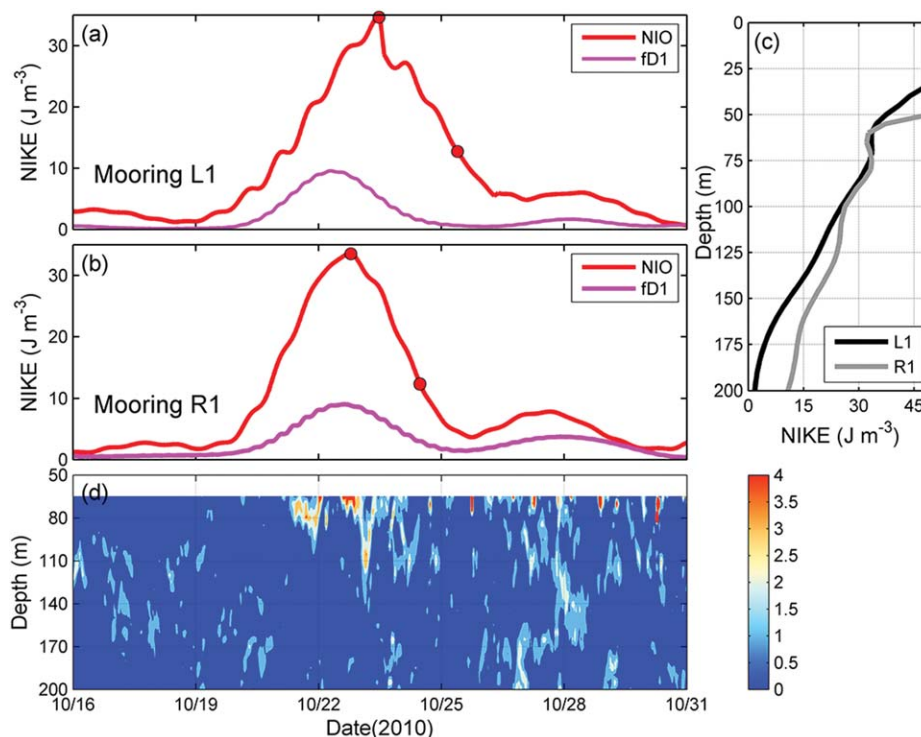
Figure 8. Period-smoothed and depth-averaged near-inertial (red), *fD1* (magenta) kinetic energy density at (a) mooring L1 and (b) R1. The red dots represent the maximum and *e*-folding value of E_f. (c) Near-inertial kinetic energy profiles when E_f in plots a and b peaked. (d) Contour of inverse Richardson number Ri^{-1} versus time and depth for mooring R1.

mooring L1 and Figure 8b for mooring R1). Under the influence of typhoon Megi, the near-inertial kinetic energy at both moorings started to increase on 20 October, then peaked in the evening of 22 October (R1) or early morning of 23 October (L1). Thereafter, the surface layer near-inertial kinetic energy damped quickly with an *e*-folding time of 1.7 days at mooring R1 and 1.9 days at mooring L1. This was a strikingly quick damping of NIOs, considering that the storm-generated NIOs could usually persist for over a week or even 10 days in the upper layer in previous studies [*Teague et al.*, 2007; *Qi et al.*, 1995]. During 26–29 October, E_f increased again under the influence of a subsequent typhoon Chaba passing east of Luzon Strait. The corresponding kinetic energy density E_{fD1} at *fD1* frequency is also shown in Figure 8. The increase and decrease of E_{fD1} were highly correlated with E_f, and its magnitude was 1/4 to 1/3 of E_f.

Generally, the damping of surface layer near-inertial kinetic energy has been related to lateral and particularly downward radiation as near-inertial internal waves [*Oey et al.*, 2008]. Unfortunately, based on our limited observations, it is difficult to estimate the lateral energy flux and hence energy loss of local NIOs. However, *Zhai et al.* [2009] demonstrated that in a three dimensional model the integrated energy flux through the open boundaries was indeed small compared to the downward radiation and generally could be neglected. Therefore, the downward energy flux was focused on in the present study. Using the method introduced in *Qi et al.* [1995], the vertical group velocity C_{gz} was first estimated based on the "Wentzel-Kramers-Brillouin (WKB)" approximation, by examining the time delay of a near-inertial wave group as it propagates vertically. If only the downward energy radiation was considered, a theoretical *e*-folding time scale T_e of surface-layer near-inertial kinetic energy (above 100 m) could be estimated via equation (7):

$$T_e = \frac{\int_{100}^{0} E_f(z)dz}{C_{gz}(100) \times E_f(100)}. \tag{7}$$

The estimated vertical group velocity C_{gz} at 100 m depth was 28.8 m d^{-1} at mooring R1 and 29.6 m d^{-1} at mooring L1, respectively. The near-inertial kinetic energy density profiles corresponding to the time when E_f
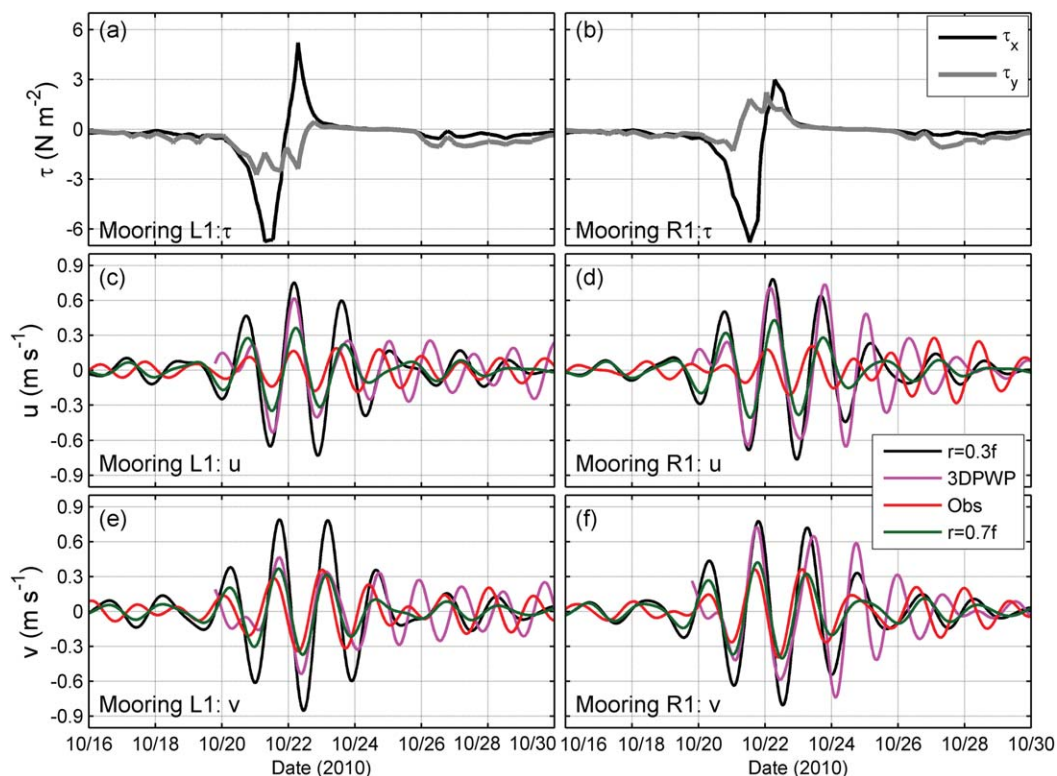
Figure 9. (top) Eastward (black line) and northward (gray line) components of wind stress at moorings (a) L1 and (b) R1. (Middle) Slab model (green line for $r = 0.7$ and black line for $r = 0.3$), 3DPWP simulated (magenta) and measured (solid line) eastward component of ML near-inertial current at (c) moorings L1 and (d) R1. (bottom) As middle plots for northward component of ML near-inertial current.

peaked in Figures 8a and 8b, are shown in Figure 8c. Given the lack of measurements, kinetic energy density above 35 m at L1 (50 m at R1) was assumed to be the same value as the top layer measured by ADCPs. Then the vertical energy flux could be estimated via $F_z = C_{gz} \times E_f$. The estimated theoretical e-folding time T_e was 5.6 days at mooring L1 and 5.4 days at mooring R1. Therefore, the downward energy radiation could account for only about one third of the surface-layer near-inertial energy damping. If the lateral energy radiation was neglected, the other two thirds of the near-inertial energy might be lost locally.

Loss of internal wave energy is thought to occur either through a spectral cascade involving wave-wave interactions or direct breaking of small scale waves [*Gregg et al.*, 2003; *Alford and Gregg*, 2001]. *Johnston and Rudnick* [2009] showed that the transition layer immediately below the ML often has a Richardson number Ri close to 1. With addition of the extra current shear by strong wind [*Brannigan et al.*, 2013], the Richardson number might reach the critical value (0.25) and trigger significant shear instability, draining near-inertial energy to mixing and damping the NIOs. The inverse Richardson number Ri^{-1} was calculated in this study via equation (8):

$$Ri^{-1} = S^2/N^2, \tag{8}$$

where S^2 and N^2 are the squared shear and buoyancy frequency, respectively. The squared shear and buoyancy frequency were calculated by taking first differences of current and density on a 5 m grid. Because of the fairly steady stratification before and after the passage of typhoon Megi (due to the effect of strong upwelling, Figure 2a), time-averaged stratifications (from 65 m (below the ML) to 200 m, using temperature and salinity data in Figures 2b and 2d) and real-time shear were used to calculate Ri^{-1}. Given the strong background current, the two CTDs moved up and down continuously, and profiled from 60 to 350 m. Figure 2d shows an averaged profile of salinity in October, calculated by averaging all recorded salinity data at each depth; a stationary vertical salinity distribution in October was assumed. We also calculated Ri^{-1} based

on stratification and shear both in real time, and the results showed that the replacement using averaged stratifications was reasonably good.

Figure 8d shows that before typhoon Megi Ri^{-1} was much smaller than 4, the critical value for onset of stratified shear flow instability. During the passage of typhoon Megi, Ri^{-1} increased and was close to or even larger than the critical value 4, indicating the occurrence of enhanced mixing and dissipation of kinetic energy. However, the occurrence of shear instability (large Ri^{-1}) also corresponded to the generation of $fD1$ and both were confined to a depth range above about 100 m (Figures 6, 8b, and 8d), suggesting an important role of $fD1$ in triggering shear instability and contributing to the enhanced mixing during typhoon Megi. Therefore, we suggest that the nonlinear wave-wave interaction between NIOs and diurnal tide drained energy away from NIOs to $fD1$ (see section 5) and finally dissipated locally, and hence significantly accelerated the damping of NIOs under typhoon Megi.

4.2. Model Experiments

The 3DPWP model was used to simulate the three-dimensional ocean response to typhoon Megi, without tides. As in *Sanford et al.* [2011], the ocean initial condition is taken to be a state of rest, homogeneous horizontally, and with vertical temperature and salinity profiles observed by temperature-chains preMegi (Figures 2b and 2d). The model-simulated ML near-inertial currents, at moorings L1 and R1, were extracted via a fourth-order Butterworth filter by employing the same bandwidth used in section 3.2, and compared in detail with the observed top-layer near-inertial current from ADCPs in Figure 9. At both moorings R1 and L1, the 3DPWP simulated NIOs were generally in phase with those observed by ADCPs. However, the model-simulated NIOs were more than two times larger than observation and persisted for more than 4 inertial periods in the ML. Considering that the lateral, downward radiation and local dissipation processes had all been accounted for in the 3DPWP model, it was striking that the observed NIOs were relatively weak and quickly damped, implying that other processes may affect the upper ocean current response to Megi.

The slab model was used to simulate and further examine the relatively weak and more quickly damped NIOs generated by typhoon Megi in the northern SCS. The pretyphoon ML depth H was assumed to be 60 m based on the estimation in section 3.1. In the slab model, r^{-1} is referred to as the *e*-folding time of the simulated near-inertial current, so a large value of r generally corresponds to small amplitude of the simulated near-inertial current. The value of r is empirically defined. By matching the simulated and observed near-inertial currents, *Alford* [2001] suggested r to be $(0.1–0.3)f$; when $r = 0.15f$ his simulations and measurements had the best correlation.

In this study, we first took $r = 0.3f$ (corresponding to an *e*-folding time of about 3.3 inertial periods), the upper limit suggested by *Alford* [2001]. During the passage of typhoon Megi, although the simulated near-inertial current matched the measurements well in phase at both moorings L1 and R1, a much larger amplitude (>0.8 m s^{-1}) was simulated than measured (only about 0.4 m s^{-1}). If a much larger value of $r = 0.7f$ was taken (corresponding to an *e*-folding time of about 1.5 inertial periods, similar to that observed in section 3.2), the simulated near-inertial currents correlated much better with measurements both in phases and amplitudes, especially for v components. Therefore, the value of r was critical in reproducing the NIOs under typhoon Megi and a much larger value of r was required to damp the near-inertial current more quickly.

Both the results of the 3DPWP and slab model experiments suggested that, along with the commonly considered lateral and downward energy radiation, an additional dissipation process was required in the northern SCS to damp the NIOs more quickly. As suggested in Figure 8, energy transfer from NIOs to higher frequency internal waves such as $fD1$ via a nonlinear wave-wave interaction triad (section 5), with accompanying critical Ri^{-1} (section 4.1), may account for the rapid local dissipation of typhoon-generated NIOs and limit the growth of ML NIOs.

5. Nonlinear Wave-Wave Interaction

5.1. Wavelet Analysis

Wavelet analysis was used to examine the energy evolution of the nonlinear wave-wave interaction triad, NIO, diurnal tide, and $fD1$ (Figure 10). Consistent with the power spectral analysis in section 3.2, the northward component of observed top-layer currents at moorings L1 and R1 were used to construct Figure 10.
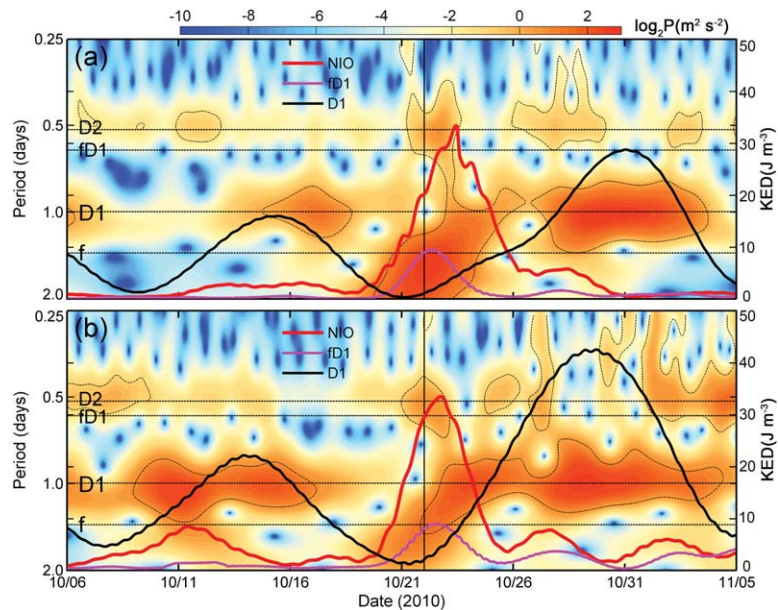
Figure 10. Wavelet power spectrum (color; $m^2\ s^{-2}$) of northward current components for (a) moorings L1 at 40 m depth and (b) R1 at 55 m depth. The vertical line represents the time when typhoon Megi passed. The f, $D1$, $fD1$, and $D2$ frequencies are indicated as horizontal lines. The period-smoothed and depth-averaged (above 100 m) kinetic energy density was also overplotted for NIO, $D1$, and $fD1$, and the scales are indicated at the right axis ($J\ m^{-3}$). The depth-averaged diurnal kinetic energy density was divided by 2 for better presentation and comparison with that of f and $fD1$.

Moreover, the period-smoothed kinetic energy density of NIO, $D1$, and $fD1$ are overplotted in Figure 10 (as depth averages above 100 m, consistent with Figure 8).

Figure 10 illustrates the intermittent nature of near-inertial energy as well as the intermittent energy at $fD1$ frequency. Before typhoon Megi (6–21 October), energy at near-inertial and $fD1$ frequencies was extremely weak. During the passage of Megi (21–24 October), energy at near-inertial and $fD1$ frequencies increased synchronously and a strong energy peak exceeding the 95% confidence level at the frequency $fD1$ appeared. During the subsequent strong winds (26–28 October, up to 18 m s^{-1}, Figure 9a and 9b; 1–5 November, not shown), elevated energy was also observed at both the near-inertial and $fD1$ frequencies. It is notable that the transient energy bursts at the f and $fD1$ frequencies were strongly correlated in time (but not diurnal tide $D1$). The existence of the significant energy peak at the sum frequency of f and $D1$ (Figures 3 and 10) and its high correlation with NIOs, in the absence of any other known forcing at $fD1$ frequency, implies that the NIOs forced the $fD1$ via nonlinear wave-wave interaction with the diurnal tide.

It was striking that the diurnal tide was still able to dominate the internal wave band, and the surface-layer diurnal energy during the spring tide after Megi was more than twice that before the typhoon. The surface-layer intensification of diurnal tides after typhoon Megi will be discussed in detail in section 6.

5.2. Nonlinear Momentum Terms

Nonlinear wave-wave interaction has long been considered to be the physical mechanism of energy transfer through the internal wave continuum. For an interaction triad, two primary waves provide forcing for a third wave at their sum or difference frequency. In this study, the secondary wave $fD1$ could be forced by the coupling of NIOs and diurnal tide via equations (9) and (10):

$$\frac{\partial u_{fD1}}{\partial t} \approx -\left(u\frac{\partial u}{\partial x}\right)_{fD1} - \left(v\frac{\partial u}{\partial y}\right)_{fD1} - \left(w\frac{\partial u}{\partial z}\right)_{fD1}, \tag{9}$$

$$\frac{\partial v_{fD1}}{\partial t} \approx -\left(u\frac{\partial v}{\partial x}\right)_{fD1} - \left(v\frac{\partial v}{\partial y}\right)_{fD1} - \left(w\frac{\partial v}{\partial z}\right)_{fD1}, \tag{10}$$

Xing and Davies [2002] and *Davies and Xing* [2003] used a three-dimensional model to investigate the nonlinear interaction between NIO and M2 internal tide at a shelf edge and concluded that the occurrence of
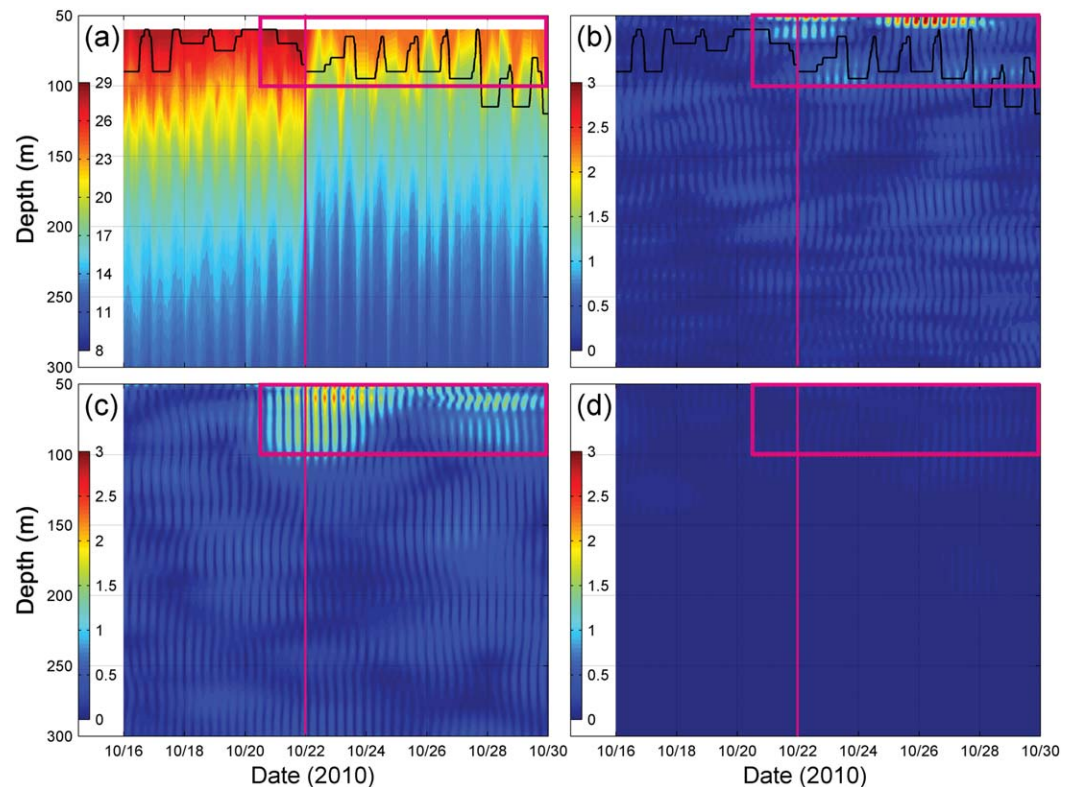
Figure 11. (a) Contours of temperature (°C) versus time and depth after extrapolating at mooring R1; (b) amplitude of vertical nonlinear terms (10^{-5} m s^{-2}); (c) amplitude of time derivative of *fD1* current (10^{-5} m s^{-2}); (d) amplitude of horizontal nonlinear terms (10^{-5} m s^{-2}). The vertical solid lines represent the time when typhoon Megi passed. The solid black curve in plots a and b indicates the depth above which the temperature was obtained via extrapolation. Red rectangles indicate the two events of *fD1*.

fM2 was mainly associated with the shear in the NIO and the vertical velocity due to M2 internal tide, i.e., the vertical nonlinear momentum terms $-w\frac{\partial u}{\partial z}$ and $-w\frac{\partial v}{\partial z}$ in equations (9) and (10).

In the present study, to examine the relative importance of the various nonlinear processes giving rise to energy at *fD1* frequency, the time derivative of *fD1* velocity (left side of equations (9) and (10)), and the horizontal and vertical nonlinear momentum terms (right side of equations (9) and (10)) were calculated and compared (Figure 11). Moorings L1 and R1 were nearly at the same latitude (Table 1), so only the x derivative of the current could be estimated for horizontal nonlinear terms $\left(-u\frac{\partial u}{\partial x}, -u\frac{\partial v}{\partial x}\right)$. The nonlinear terms $\left(-v\frac{\partial u}{\partial y}, -v\frac{\partial v}{\partial y}\right)$ with the northward component of horizontal advection could not be estimated and were thought to have amplitude comparable with $\left(-u\frac{\partial u}{\partial x}, -u\frac{\partial v}{\partial x}\right)$.

To estimate the vertical nonlinear terms $\left(-w\frac{\partial u}{\partial z}, -w\frac{\partial v}{\partial z}\right)$, vertical velocity w was first calculated as the time derivative of the vertical displacements of isopycnals η (equation (11)):

$$w = \frac{\partial \eta}{\partial t}, \tag{11}$$

where η was defined to be the vertical displacement of an isopycnal because of internal waves etc., relative to its average depth during a longer period (such as 15 days in this work, from 16 to 30 October). The temperature from the moored chains and salinity recorded by the two CTDs at mooring R1 were used in estimating density profiles to derive η. The estimation of vertical velocity w was significantly limited by the data gap of temperature in upper layers, particularly after typhoon Megi (Figure 2a). Thus, the temperature data set was first extrapolated from the observed lower layers (approximately 80 m before typhoon and 100 m after) up to 60 m during the needed time duration (16–30 October; Figure 11a). The estimation of vertical velocity w and its required extrapolation of temperature from observations are described in Appendix A.
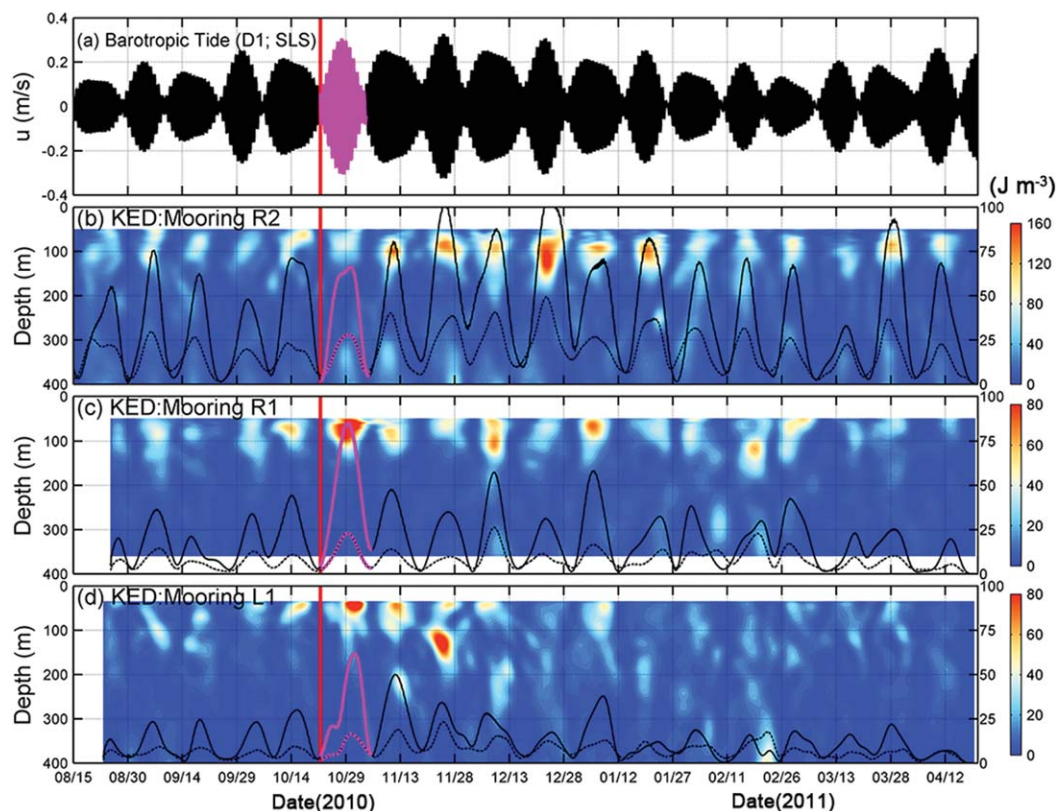
Figure 12. (a) Eastward component of diurnal barotropic tide at Luzon Strait (SLS in Figure 1); (b–d) The diurnal kinetic energy density at mooring R2, R1, and L1. The solid and dotted lines stand for depth-averaged E_{D1} above 100 m and over the entire observed water column, respectively, and the scales are indicated at the right axis. Spring tides just after the typhoon Megi are emphasized in magenta. The vertical red lines represent the time when typhoon Megi passed.

The time series of nonlinear terms at *fD1* frequency was band-pass filtered by employing the same band (1.47–1.77 cpd) used in section 3.2. The amplitude of the time derivative of *fD1* velocity $\left(\sqrt{\left(\frac{\partial u_{fD1}^{fD1\,fD1}}{\partial t}\right)^2 + \left(\frac{\partial v_{fD1}^{fD1\,fD1}}{\partial t}\right)^2} \right)$, the horizontal $\left(\sqrt{\left(u\frac{\partial u}{\partial x}\right)^2_{fD1} + \left(u\frac{\partial v}{\partial x}\right)^2_{fD1}} \right)$ and vertical nonlinear terms $\left(\sqrt{\left(w\frac{\partial u}{\partial z}\right)^2_{fD1} + \left(w\frac{\partial v}{\partial z}\right)^2_{fD1}} \right)$ forcing *fD1* are shown in Figure 11. As for the highly intermittent *fD1* events and hence the time derivative (Figure 11c), the vertical nonlinear momentum term presents the same intermittency with large values during 21–24 and 26–28 October (Figure 11b). Generally, the vertical nonlinear terms have the same amplitude and variations (temporal and vertical; large values were confined in the upper 100 m) as those of time derivative of *fD1* velocity, while the amplitude of horizontal nonlinear terms was more than 10 times smaller (Figure 11d). This suggests that the occurrence of *fD1* was mainly forced by the vertical nonlinear momentum terms $\left(-w\frac{\partial u}{\partial z}, -w\frac{\partial v}{\partial z} \right)$, which relate to the vertical shear in near-inertial motion NIO and vertical velocity of diurnal internal tide *D1*, or the vertical shear of *D1* and vertical velocity of the NIO. These results were robust to different extrapolation methods for temperature and vertical velocity described in Appendix A.

6. Burst of Surface-Layer Diurnal Energy after Megi

As shown in section 3.2 and Figure 10, both current velocity spectra and filtered current velocity indicated a significant enhancement of surface-layer diurnal energy at moorings L1 and R1 after the passage of typhoon Megi. This dramatic enhancement was thought to be related to the passage of typhoon Megi. The diurnal kinetic energy density E_{D1} (Figure 12) was estimated via equation (6) with the filtered diurnal current.

Figures 12c and 12d show the (24 h smoothed) kinetic energy density E_{D1} for the entire observed duration (longer than 7 months) at moorings R1 and L1. After typhoon Megi, the diurnal kinetic energy density increased over the entire observed depth range. However, a more dramatic increase up to 100% appeared in the upper 100 m. Depth-averaged E_{D1} above 100 m shows that the spring tide just after the passage of Megi was the most intense one during the 7 month recordings and dramatically 2–4 times larger than others. Therefore, it seems that a burst of surface-layer (above 100 m) diurnal energy appeared following the passage of typhoon Megi.

6.1. Relation to the Barotropic Tide at Luzon Strait

The diurnal internal tide in the SCS is commonly thought to be generated at Luzon Strait by barotropic tidal currents flowing over seamounts and to propagate westward into the SCS. Thus, the relation of the surface-layer diurnal energy burst with the variability of the barotropic tide at Luzon Strait was first examined. Taking the source region at Luzon Strait (SLS in Figure 1) with the same position as *Ramp et al.* [2010], the eastward component of barotropic diurnal tidal currents, predicted from the Oregon State Ocean Topography Experiment (TOPEX)/Poseidon 7.2 (TPXO7.2) tidal inverse model [*Egbert and Erofeeva*, 2002], was extracted corresponding to the 7 months observations in the SCS and is presented in Figure 12a (including the four primary constituents K1, O1, P1, and Q1).

At moorings R2, R1, and L1, the variability of diurnal energy (both of the depth averaged E_{D1} above 100 m and over the entire observed depth range) in the SCS follows the variability of barotropic tide at the source region (SLS) quite well, gradually increasing from August to December 2010 and then decreasing until March 2011. The correlation between the source region barotropic tide and the SCS diurnal energy gradually decreases when the internal tide propagates even further away from Luzon Strait, because the internal tide interacts with background conditions and integrates their effects through variable stratification and mesoscale activity after a long propagation [*Park et al.*, 2006].

An obvious exception appeared during the spring tide at mooring R1 and L1 after the passage of typhoon Megi: the burst of surface-layer diurnal energy. Compared with the other spring tides pre-Megi or more than 15 days post-Megi, the spring tide just after typhoon Megi had moderate barotropic tide intensity at Luzon Strait and moderate intensity E_{D1} depth-averaged over the entire observed depth range, but a much larger surface-layer diurnal energy at moorings R1 and L1; that at mooring R2 had no difference from other cases. Therefore, the burst of surface-layer diurnal energy could not be attributed to the variability of barotropic tides at Luzon Strait, but probably to the passage of typhoon Megi.

6.2. Stratification Change

Internal waves adjust their amplitude and energy (exhibiting $E(z) \sim N(z)$, following *Leaman and Sanford* [1975]) when they undergo refraction in variable stratification. Modeling experiments suggested that local stratification change influenced by winds could modify the vertical distribution of internal tides [*Hall and Davies*, 2007]. Using current data from mooring observations, *Xu et al.* [2012] confirmed that the vertical distribution of internal tidal energy can be strongly modulated by changing stratification. By processes such as upwelling and mixing via shear instability, a typhoon can significantly affect and modulate the evolution of temperature and stratification in the upper ocean. Strong upwelling and cooling over the entire observed water column from 60 to 360 m were observed under typhoon Megi and persisted for about 20 days (Figure 2a). Time averaged temperature profiles at mooring R1 during the spring tides pre-Megi (14–17 October) and post-Megi (25–29 October, slightly earlier than the spring tide because of the lack of temperature data later, Figure 2a) were calculated and are shown in Figure 13a. An averaged salinity profile (Figure 2d) was assumed in calculating the squared Brunt-Väisälä frequencies (N^2) at 5 m vertical scale (Figure 13b). Figure 13b shows that the stratification became significantly stronger above 100 m after typhoon Megi. There may be two reasons for the enhanced surface-layer stratification: (1) because of the enormous upwelling pumped by Megi wind stress, the ML became shallower and the maximum temperature drop occurred at 100 m (Figure 2c) but not in the ML, resulting in more intense cooling in the thermocline than in the ML and leading to stronger stratification; (2) through the surface heat flux of solar radiation, the ML warms faster than the underlying thermocline; this may further intensify the temperature gradient at the ML base and upper thermocline.

The time-averaged kinetic energy density profiles $E_{D1}(z)$ were calculated during the spring tides before (14–17 October) and after (28–31 October) the passage of typhoon Megi and are presented in Figure 13c. The
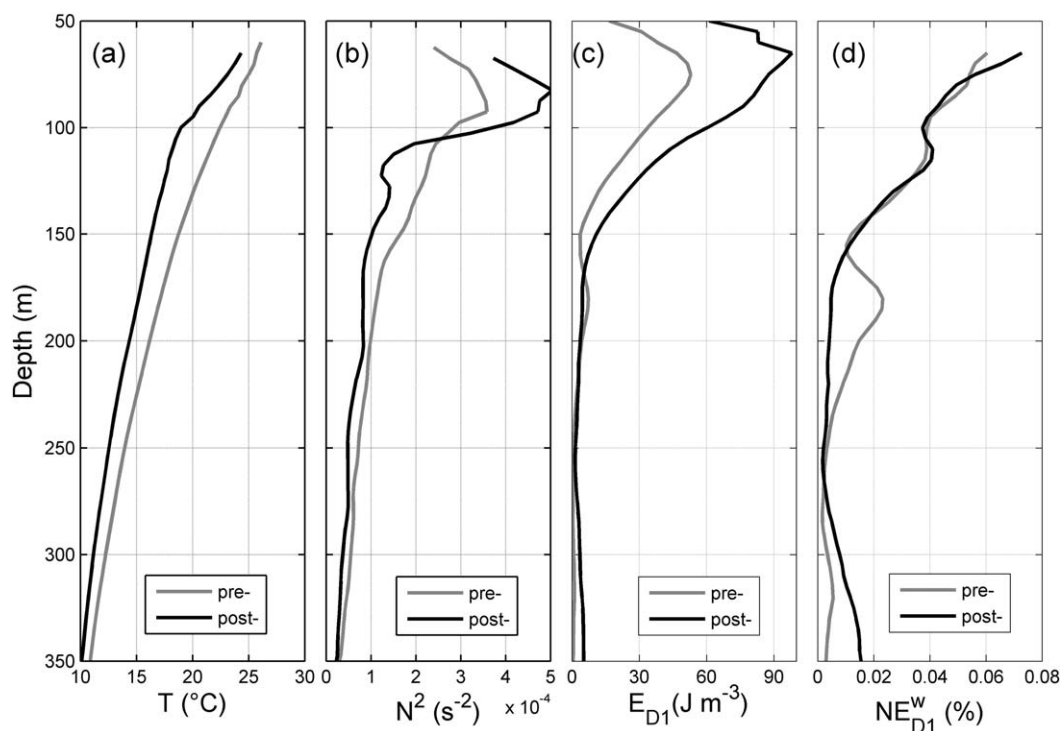
Figure 13. Time-averaged profiles of (a) temperature; (b) squared Brunt–Väisälä frequency; (c) diurnal kinetic energy density E_{D1}; and (d) normalized WKB scaled diurnal kinetic energy density NE_{D1}^{w} during the spring tides before (gray line) and after (black line) typhoon Megi.

diurnal energy increased over nearly the entire observed water column, and this may be related to the larger barotropic diurnal tide at Luzon Strait (Figure 12a). However, corresponding to the enhanced surface-layer stratification, a striking energy increase appeared in the surface layer (mostly above 100 m), which is probably due to the stronger stratification induced by typhoon Megi. To demonstrate this, a WKB scaling was used to minimize the refraction effect [*Leaman and Sanford*, 1975]. The WKB-scaled diurnal kinetic energy E_{D1}^{w} was calculated via equation (12):

$$E_{D1}^{w}(z) = \frac{\overline{N}}{N(z)} E_{D1}(z). \tag{12}$$

To further eliminate the effect of increased barotropic tide at Luzon Strait, the normalized kinetic energy density profiles NE_{D1}^{w} were estimated via equation (13) and are shown in Figure 13d:

$$NE_{D1}(z) = \frac{E_{D1}^{w}(z)}{\displaystyle\int_{350}^{50} E_{D1}^{w}(z)\,dz}. \tag{13}$$

When taking the WKB scaling into account, the surface intensified diurnal energy would generally disappear (Figure 13d), validating the effect of stronger stratification in amplifying the surface diurnal energy after typhoon Megi. Another energy peak appeared at ~180 m depth before the typhoon, probably because of the modulation of different modes or energy concentration for some other reason, but this was not the focus in the present work. Therefore, typhoon Megi enhanced the stratification of the surface-layer and amplified the surface-layer diurnal internal tidal current, resulting in the dramatic burst of surface-layer diurnal energy during the spring tide after Megi.

6.3. Wind-Generated Diurnal Current
Simpson et al. [2002] suggested that forced diurnal oscillations could be generated by wind with significant energy at diurnal frequency in oceans close (±10°) to the diurnal critical latitude (~29°). In the slab model,
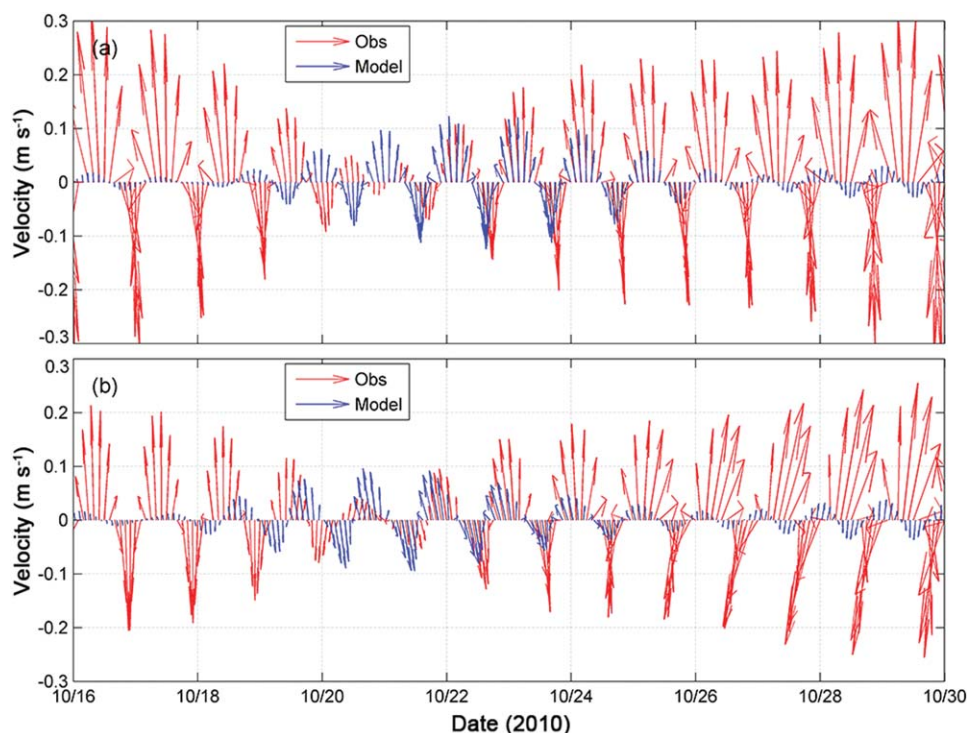
Figure 14. Observed (red) and slab-model-simulated (blue) diurnal current presented as arrows for moorings (a) L1 and (b) R1.

most of the wind generated currents were near the inertial frequency, but currents at other frequencies could also be generated due to the broad-band distribution of wind energy. Therefore, the current in the slab model was band-pass filtered with the same diurnal band (0.86, 1.09)$K1$ as in section 3.2.

Figures 14a and 14b show the wind-generated diurnal currents via the slab model, compared with ADCP-measured top-layer diurnal currents at mooring L1 (35 m) and R1 (50 m). Before typhoon Megi, the simulated diurnal current was extremely weak due to the slight winds, and it gradually increased to about 0.1 m s^{-1} during the passage of Megi, and then decreased again after the typhoon. It is notable that from 21 to 27 October, the simulated wind-generated diurnal current was nearly in phase with the observed diurnal tidal current, indicating that the typhoon wind might reinforce the diurnal energy in the surface layer. Thus, we suggest that the wind forcing may be another cause of the dramatic burst of surface-layer diurnal energy during the spring tide after Megi, in addition to the surface intensification of stratification.

7. Discussion and Conclusions

Preexisting ocean background features could significantly modulate the upper ocean response to TCs. The northern SCS, with multiscale motions present including the large scale circulation, mesoscale eddies as well as the strong internal tides, etc., has an even more complex background condition than open oceans. However, due to insufficient observation data, investigations of the upper ocean response to typhoons in the northern SCS have been limited. In the present study, the upper ocean response to typhoon Megi (2010) was carefully examined in the northern SCS with strong diurnal internal tides present based on the observed ocean current and temperature data sets from two subsurface moorings.

Compared with the NIO response to Atlantic hurricane Frances with the same category 3, a relatively weak and quickly damped NIO was observed under typhoon Megi (2010) in the northern South China Sea, with a maximum near-inertial velocity approximately 0.4 m s^{-1} in the ML, and a short decay time scale within 2 inertial periods (Figure 5). Moreover, a significant energy peak at the $fD1$ frequency appeared after the passage of typhoon Megi, indicating an enhanced nonlinear wave-wave interaction between NIO and the diurnal tide. After Megi, the surface-layer diurnal energy was also enhanced by up to 100%.

Previous studies demonstrated that the amplitude of typhoon-generated NIO was determined by several key factors, including the pretyphoon ML depth, magnitude of wind stress, and proximity of the wind vector rotation (related to the translation speed of typhoon) to the local inertial frequency [*Crawford and Large*, 1996; *Jaimes and Shay*, 2010]. In spite of the relatively slow translation speed of typhoon Megi, the ML NIO simulated by both the 3DPWP and slab models ($r = 0.30$) was more than twice as large as the observations at both moorings L1 and R1 with a realistic pretyphoon ML depth. Assuming a much quicker damping of the NIO in the slab model ($r = 0.70$), the ML NIOs were reproduced fairly well at both moorings L1 and R1. Downward energy radiation of near-inertial internal waves accounted for about one third of the surface-layer near-inertial energy damping, and the other two thirds of the energy was lost locally with an *e*-folding time less than 2 days. This quick damping of NIOs was demonstrated to be related to the energy transfer to *fD1* via nonlinear wave-wave interaction between NIOs and diurnal tides, particularly as it was neap diurnal tides during the passage of Megi (Figure 10), so the energy transferred to *fD1* waves (Figure 6; with velocity amplitude up to 0.2 m s^{-1}, nearly half that of the NIOs) might have been mainly from the NIOs. Thus, the nonlinear interaction and energy transfer to *fD1* may have limited the growth of the mixed-layer NIOs, resulting in the relatively weak and quickly damped NIO under typhoon Megi in the northern SCS.

Given the permanent existence of diurnal internal tides in the northern SCS, wavelet analysis indicated a strong correlation between NIO and *fD1* (Figure 10), implying that a forced nonlinear wave-wave nonresonant interaction might be responsible here between NIO and diurnal tides [*Mihaly et al.*, 1998]. Among the nonlinear interactants with the M2 internal tide found in the SCS [*Xie et al.*, 2008, 2011], NIO interacting with the diurnal tide under a typhoon is presented this study. This interaction may play an important role in energy cascading through the internal wave continuum and in modulating the mixing in the SCS.

Although there may be some errors in the extrapolation of temperature, experiments with different extrapolation methods indicated that the calculated results of nonlinear momentum terms, which forced the *fD1*, were robust to different extrapolation methods, implying a realistic physical process rather than a numerical artifact. The calculated vertical nonlinear terms had intermittency and vertical distribution similar to the time derivative of *fD1* current, and were more than 10 times larger than the horizontal nonlinear terms, suggesting that the occurrence of *fD1* was mainly forced by the vertical nonlinear momentum terms $\left(-w\frac{\partial u}{\partial z}, -w\frac{\partial v}{\partial z}\right)$. Furthermore, the vertical nonlinear term $-w\frac{\partial u}{\partial z}$ for the triad of interactants *f* (NIO), *D1* and *fD1* can be decomposed into two terms, $-w_{D1}\frac{\partial u_f}{\partial z}$ (vertical shear of NIO and vertical velocity of *D1*), and $-w_f\frac{\partial u_{D1}}{\partial z}$ (vertical shear of *D1* and vertical velocity of NIO). In the numerical experiments of *Xing and Davies* [2002], only the $-w_{D1}\frac{\partial u_f}{\partial z}$ term (with M2 in their study instead of D1) gave rise to substantial energy of the secondary wave, because of the strong shear from the simulated near-inertial on-offshore oscillatory flow and relatively weak vertical velocity w_f in the other term $-w_f\frac{\partial u_{D1}}{\partial z}$. In the present study, considerable near-inertial internal wave energy and hence inertial pumping were generated under typhoon Megi (Figures 2a and 5), so the terms $-w_f\frac{\partial u_{D1}}{\partial z}$ and $-w_{D1}\frac{\partial u_f}{\partial z}$ had similar amplitudes (not shown) and both substantially contributed to the energy transfer to *fD1*.

After the passage of typhoon Megi, the surface-layer diurnal energy was significantly enhanced and it seems that a burst of surface-layer diurnal energy appeared during the subsequent spring tide. The relation between the burst of surface-layer diurnal energy and the variations of barotropic tide at the source region Luzon Strait was first examined. Theoretically, linear internal tide generation predicts that the intensity of the generated internal tides over the entire water column is linearly proportional to the strength of tidal forcing at the generation site [*Vlasenko et al.*, 2005]. In the present study, the barotropic tide at Luzon Strait increased by only 40% compared with the spring tide before the typhoon; however, the surface-layer diurnal energy increased by up to 100% at both moorings R1 and L1 after Megi. Therefore, the burst of surface-layer diurnal energy was not related to the variability of the barotropic tide at Luzon Strait, but probably to the passage of Megi. The variability of upper-layer structure of the water column could be important in affecting propagation characteristics of the internal tide [*Shaw et al.*, 2009]. After the passage of typhoon Megi, the stratification increased above 100 m and decreased below, with a similar change of the vertical distribution of diurnal energy density, so it seems that the enhanced surface-layer stratification changed the vertical distribution of diurnal energy and amplified the surface-layer diurnal energy (Figure 13).

The common phase of slab-model-simulated and observed diurnal currents implied that the wind further reinforced the surface diurnal current postMegi (Figure 14). However, some uncertainties may exist related to the uncertainties in the modeled wind field and ML depth *H* in the model. Given the dominant first-

mode diurnal internal tide in the northern SCS [*Xu et al.*, 2012], the velocity seems to have the same phase through the upper ocean (from surface to at least 150 m; Figure 7). Thus it seems that a ML deeper than 60 m should be adopted for the diurnal current simulation in the slab model. However, a larger value of H would decrease the amplitude but not change the phase of simulated diurnal current, so we suggest that the typhoon wind did reinforce the surface diurnal current, but it cannot be estimated quantitatively by the simple slab model.

The present study provides a suggestive and intriguing insight on the upper-ocean response to typhoons in the northern SCS with a complex background. However, we caution that the present work was a case study under one typhoon and an incomplete sample of current and temperature data were recorded by the two moorings. Further study, based on more concurrent atmospheric and oceanic in situ observations and more sophisticated three-dimensional numerical models, is required to examine the modulation by complex background conditions of upper-ocean response to typhoons in the SCS.

Appendix A: Extrapolation Method of Temperature Data Set

The temperature data gap in the upper layers was filled in via extrapolating the data from the observed lower layers up to 60 m (Figure 11a). The extrapolation method was as follows: (1) The time variation of temperature at each depth was assumed to result from a reference temperature profile moving up and down due to internal waves, and the depth difference of nearby isotherms did not change during a short time interval. (2) Because of the strong upwelling due to typhoon Megi, two averaged temperature profiles were estimated as the reference temperature profiles (Figure 2b) for pre-typhoon (16–21 October) and post-typhoon (22–30 October) conditions, respectively. (3) According to the reference temperature profiles and unchanging depth difference of nearby isotherms, the data gap was filled in via extrapolating the temperature from the observed lower layers up to 60 m (Figure 11a). Thus, the evolution of isopycnals and hence vertical velocity w (by equation (11)) from 60 to 350 m was estimated. For simplicity, values of w from 50 to 55 m were assumed to be the same as at 60 m depth when calculating vertical nonlinear terms in Figure 11b.
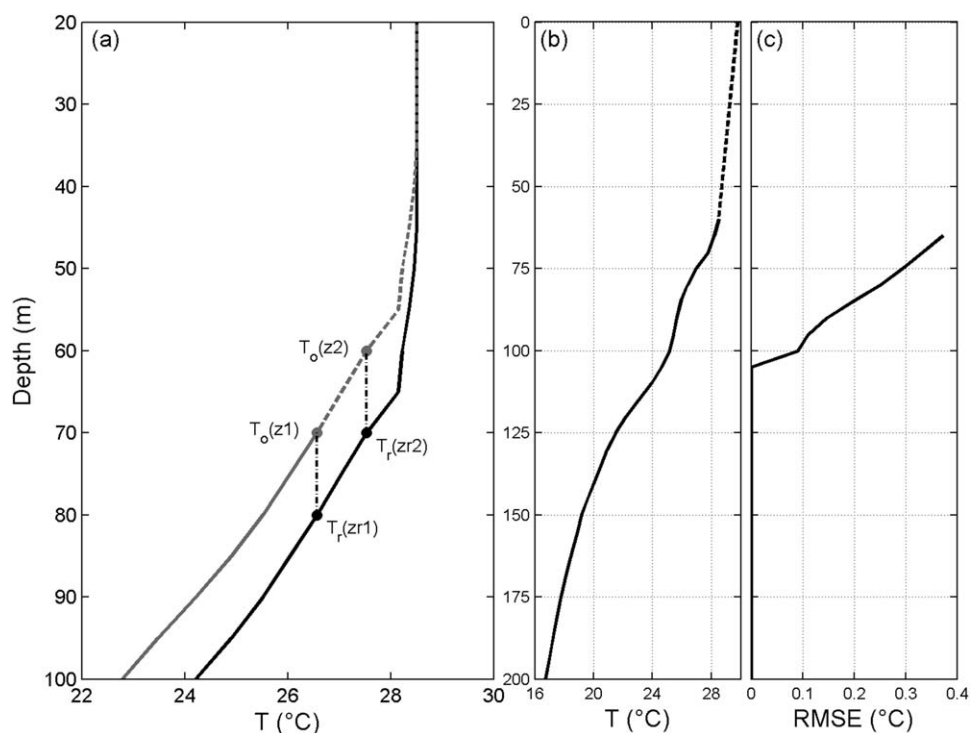
Figure A1. (a) Schematic for the extrapolation method. Temperature profiles $T_r(z)$ and $T_o(z)$ are shown as gray and black lines, respectively. Extrapolated data of $T_o(z)$ is plotted as a dashed line. (b) Averaged temperature profile from Figure A2b. As in Figure A2b, the satellite observed SST is used as a "cap" in the calculation and linked directly by dashed line with the observed top-layer temperatures. (c) RMSE profile for the extrapolation.
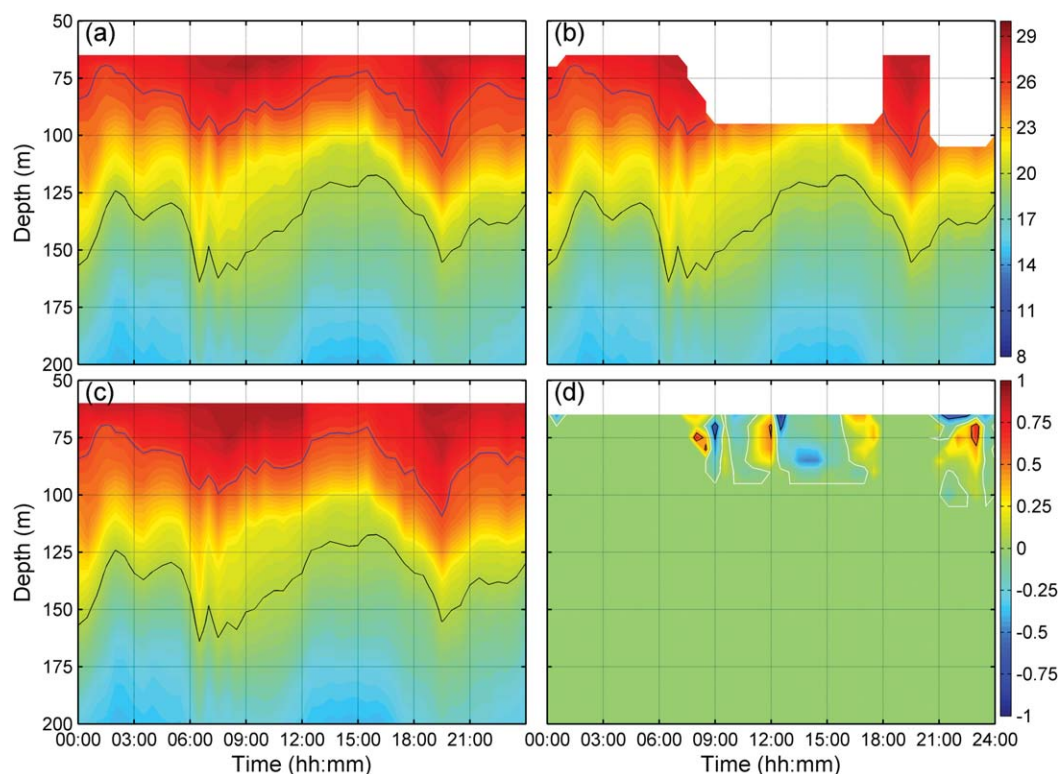
Figure A2. (a) Observed raw temperature data set; (b) temperature data set after some data were removed from plot a; (c) extrapolated temperature data set; (d) temperature difference between plots a and c. The 20°C, 26°C isothermal lines are plotted with black and blue lines, respectively. Note the different color scales for Figures A2a–c and Figure A2d.

A schematic in Figure A1a demonstrates the extrapolation method in detail. The extrapolation of temperature was performed as follows: (1) A time-averaged temperature profile was estimated as the reference profile $T_r(z)$ (gray line in Figure A1). (2) An observed temperature profile $T_o(z)$ with no data above z_1 (corresponding temperature $T_o(z_1)$) was considered. (3) The depth z_{r1} at which $T_o(z_1)$ occurs in the reference profile $T_r(z)$ was indentified. (4) Calculate temperature $T_r(z_{r1} + z_2 - z_1)$. (5) Given the assumption of unchanging depth difference between nearby isotherms when the reference profile $T_r(z)$ moves up and down, $T_o(z_2) = T_r(z_{r1} + z_2 - z_1)$. (6) Based on $T_o(z_2)$, repeat steps (3) to (4), and the temperature of higher layers could be obtained.

The extrapolation method was evaluated using a data set for 1 day when the data from 65 to 350 m (Figure A2a) have been fully measured. Data gaps in the upper layers were produced in Figure A2b by artificially removing certain data in Figure A2a. Using the aforementioned method, the temperature data in Figure A2b were extrapolated and shown in Figure A2c (reference temperature as shown in Figure A1b). The extrapolated temperature effectively reproduces the raw data and captures most variations of the isotherms. The temperature difference between Figures A2a and A2c is shown in Figure A2d. The difference was generally less than 0.5°C. As shown in Figure A1c, the root-mean-square errors (RMSE) increase upward because the extrapolation was performed upward layer by layer, accounting for the larger top-layer errors in Figure 11b.

Besides the extrapolation method described above, another three methods were adopted to examine the errors in calculating vertical nonlinear terms from the imprecise estimation of vertical velocity w in the upper-layer gaps. These three alternative methods are as follows: (1) extrapolating temperature from top-layer observations to 60 m directly. (2) assuming that the vertical velocity in the upper-layer gaps was the same as in the top observed layer, (3) extrapolating the vertical velocity from the observed top layer to 50 m *via* an empirical upward decrease based on the observed data from 65 to 100 m. Despite the slight difference in amplitudes, all results suggested almost the same temporal and vertical variation as in Figure 11b. This implies that the results were essentially robust to different extrapolation methods and we

did capture the main structure and variation of the vertical nonlinear momentum terms, although certain errors may occur in estimating the vertical nonlinear terms (e.g., the calculated amplitude at 50–60 m from 26 to 28 October was larger than that during 21–24 October, despite the weaker $fD1$).

References

Alford, M. H. (2001), Internal swell generation: The spatial distribution of energy flux from the wind to mixed layer near-inertial motions, *J. Phys. Oceanogr.*, *31*, 2359–2368.

Alford, M. H. (2008), Observations of parametric subharmonic instability of the diurnal internal tide in the South China Sea, *Geophys. Res. Lett.*, *35*, L15602, doi:10.1029/2008GL034720.

Alford, M. H., and M. Gregg (2001), Near-inertial mixing: Modulation of shear, strain and microstructure at low latitude, *J. Geophys. Res.*, *106*, 16,947–16,968.

Alford, M. H., R.-C. Lien, H. Simmons, J. Klymak, S. Ramp, Y. J. Yang, D. Tang, and M.-H. Chang (2010), Speed and evolution of nonlinear internal waves transiting the South China Sea, *J. Phys. Oceanogr.*, *40*, 1338–1355, doi:10.1175/2010JPO4388.1.

Bloomfield, P. (2000), *Fourier Analysis of Time Series: An Introduction*, 2nd ed., 261 pp., John Wiley, N. Y.

Brannigan, L., Y.-D. Lenn, T. P. Rippeth, E. McDonagh, T. K. Chereskin, and J. Sprintall (2013), Shear at the base of the oceanic mixed layer generated by wind shear alignment, *J. Phys. Oceanogr.*, *43*, 1798–1810.

Chan, J. C. L., and J. E. Shi (1996), Long-term trends and interannual variability in tropical cyclone activity over the western North Pacific, *Geophys. Res. Lett.*, *23*, 2765–2767.

Chang, S., and R. Anthes (1978), Numerical simulations of the ocean's nonlinear baroclinic response to translating hurricanes, *J. Phys. Oceanogr.*, *8*, 468–480.

Chiang, T.-L., C.-R. Wu, and L.-Y. Oey (2011), Typhoon Kai-Tak: An ocean's perfect storm, *J. Phys. Oceanogr.*, *41*, 221–233.

Chen, F., Y. Du, L. Yan, D. Wang, and P. Shi (2010), Response of upper ocean current to typhoons at two ADCP moorings west of the Luzon strait, *Chin. J. Oceanol. Limnol.*, *28*, 1002–1011.

Chen, G., H. Xue, D. Wang, and Q. Xie (2013), Observed near-inertial kinetic energy in the northwestern South China Sea, *J. Geophys. Res.*, *118*, 4965–4977, doi:10.1002/jgrc.20371.

Crawford, G. B., and W. G. Large (1996), A numerical investigation of resonant inertial response of the ocean to wind forcing, *J. Phys. Oceanogr.*, *26*, 873–891.

D'Asaro, E. A. (1985), The energy flux from the wind to near-inertial motions in the surface mixed layer, *J. Phys. Oceanogr.*, *15*, 1043–1059.

D'Asaro, E. A. (1989), The decay of wind-forced mixed layer inertial oscillations due to the b effect, *J. Geophys. Res.*, *94*, 2045–2056.

D'Asaro, E. A., T. B. Sanford, P. P. Niiler, and E. J. Terrill (2007), Cold wake of Hurricane Frances, *Geophys. Res. Lett.*, *34*, L15609, doi:10.1029/2007GL030160.

Davies, A. M., and J. Xing (2003), On the interaction between internal tides and wind-induced near-inertial currents at the shelf edge, *J. Geophys. Res.*, *108*(C3), 3099, doi:10.1029/2002JC001375.

Egbert, G. D., and S. Y. Erofeeva (2002), Efficient inverse modeling of barotropic ocean tides, *J. Atmos. Oceanic Technol.*, *19*,183–204.

Emanuel, K. A. (2005), Increasing destructiveness of tropical cyclones over the past 30 years, *Nature*, *436*, 686–688.

Garrett, C. (2001), What is the "near-inertial" band and why is it different from the rest of the internal wave spectrum?, *J. Phys. Oceanogr.*, *31*, 962–971.

Gill, A. (1984), On the behavior of internal waves in the wakes of storms, *J. Phys. Oceanogr*, *14*(7), 1129–1151.

Gregg, M. C., T. B. Sanford, and D. P. Winkel (2003), Reduced mixing from the breaking of internal waves in equatorial waters, *Nature*, *422*, 513–515.

Hall, P., and A. M. Davies (2007), Internal tide modeling and the influence of wind effects, *Cont. Shelf Res.*, *27*, 1357–1377, doi:10.1016/j.csr.2006.09.008.

Jaimes, B., and L. K. Shay (2009), Mixed layer cooling in mesoscale oceanic eddies during hurricanes Katrina and Rita, *Mon. Weather Rev.*, *137*, 4188–4207.

Jaimes, B., and L. K. Shay (2010), Near-inertial wave wake of hurricanes Katrina and Rita over mesoscale oceanic eddies, *J. Phys. Oceanogr.*, *40*, 1320–1337.

Jan, S., C.-S. Chern, J. Wang, and S.-Y. Chao (2007), Generation of diurnal K1 internal tide in the Luzon Strait and its influence on surface tide in the South China Sea, *J. Geophys. Res.*, *112*, C06019, doi:10.1029/2006JC004003.

Jarosz, E., D. A. Mitchell, D. W. Wang, and W. J. Teague (2007), Bottom-up determination of air-sea momentum exchange under a major tropical cyclone, *Science*, *315*, 1707–1709.

Johnston, T. M. S., and D. L. Rudnick (2009), Observations of the transition layer, *J. Phys. Oceanogr.*, *39*, 780–797.

Large, W. G., and S. Pond (1981), Open ocean momentum flux measurements in moderate to strong winds, *J. Phys. Oceanogr.*, *11*, 324–336.

Leaman, K. D., and T. B. Sanford (1975), Vertical energy propagation of inertial waves: A vector spectral analysis of velocity profiles, *J. Geophys. Res.*, *80*, 1975–1978.

Lin, I.-I., C. H. Chen, I. F. Pun, W. T. Liu, and C. C. Wu (2009), Warm ocean anomaly, air sea fluxes, and the rapid intensification of tropical cyclone Nargis (2008), *Geophys. Res. Lett.*, *36*, L03817, doi:10.1029/2008GL035815.

Mihaly, S. F., R. E. Thomson, and A. B. Rabinovich (1998), Evidence for nonlinear interaction between internal waves of inertial and semidiurnal frequency, *Geophys. Res. Lett.*, *25*, 1205–1208.

Niwa, Y., and T. Hibiya (2004), Three-dimensional numerical simulation of M2 internal tides in the East China Sea, *J. Geophys. Res.*, *109*, C04027, doi:10.1029/2003JC001923.

Oey, L.-Y., T. Ezer, D.-P. Wang, S.-J. Fan, and X.-Q. Yin (2006), Loop current warming by hurricane Wilma, *Geophys. Res. Lett.*, *33*, L08613, doi:10.1029/2006GL025873.

Oey, L.-Y., M. Inoue, R. Lai, X.-H. Lin, S. E. Welsh, and L. J. Rouse Jr. (2008), Stalling of near-inertial waves in a cyclone, *Geophys. Res. Lett.*, *35*, L12604, doi:10.1029/2008GL034273.

Park, J.-H., M. Andres, P. J. Martin, M. Wimbush, and D. R. Watts (2006), Second-mode internal tides in the East China Sea deduced from historical hydrocasts and a model, *Geophys. Res. Lett.*, *33*, L05602, doi:10.1029/2005GL024732.

Pollard, R. T. (1980), Properties of near-surface inertial oscillations, *J. Phys. Oceanogr.*, *10*, 385–398.

Pollard, R. T., and R. C. Millard (1970), Comparison between observed and simulated wind-generated inertial oscillations, *Deep Sea Res.*, *17*, 153–175.

Powell, M. D., P. J. Vickery, and T. Reinhold (2003), Reduced drag coefficient for high wind speeds in tropical cyclones, *Nature*, *422*, 279–283.

Price, J. F. (1981), Upper ocean response to a hurricane, *J. Phys. Oceanogr.*, *11*, 153–175.

Price, J. F. (1983), Internal wave wake of a moving storm. Part I: Scales, energy budget and observations, *J. Phys. Oceanogr.*, *13*, 949–965.

Price, J. F., R. A. Weller, and R. Pinkel (1986), Diurnal cycling: Observations and models of the upper ocean response to diurnal heating, cooling, and wind mixing, *J. Geophys. Res.*, *97*, 8411–8427.

Price, J. F., T. B. Sanford, and G. Z. Forristall (1994), Forced stage response to a moving hurricane, *J. Phys. Oceanogr.*, *24*, 233–260.

Qi, H., R. A. De Szoeke, C. A. Paulson, and C. C. Eriksen (1995), The structure of near-inertial waves during ocean storms, *J. Phys. Oceanogr.*, *25*, 2853–2871.

Ramp, S. R., Y. J. Yang, and F. L. Bahr (2010), Characterizing the nonlinear internal wave climate in the northeastern South China Sea, Nonlin. Processes Geophys., 17, 481–498, doi:10.5194/npg-17-481-2010.

Saha, S., et al. (2010), The NCEP climate forecast system reanalysis, *Bull. Am. Meteorol. Soc.*, *91*, 1015–1057, doi:10.1175/2010BAMS3001.1.

Sanford, T. B., J. F. Price, J. B. Girton, and D. C. Webb (2007), Highly resolved observations and simulations of the ocean response to a hurricane, *Geophys. Res. Lett.*, *34*, L13604, doi:10.1029/2007GL029679.

Sanford, T. B., J. F. Price, and J. B. Girton (2011), Upper-ocean response to hurricane Frances (2004) observed by profiling EM-APEX floats*, *J. Phys. Oceanogr.*, *41*, 1041–1056.

Shaw, P.-T., D. S. Ko, and S.-Y. Chao (2009), Internal solitary waves induced by flow over a ridge: With applications to the northern South China Sea, *J. Geophys. Res.*, *114*, C02019, doi:10.1029/2008JC005007.

Shay, L. K., A. J. Mariano, S. D. Jacob, and E. H. Ryan (1998), Mean and near-inertial response to Hurricane Gilbert, *J. Phys. Oceanogr.*, *28*, 858–889.

Simpson, J. H., P. Hyder, T. P. Rippeth, and I. M. Lucas (2002), Forced oscillations near the critical latitude for diurnal-inertial resonance, *J. Phys. Oceanogr.*, *32*, 177–187.

Su, J. (2004), Overview of the South China Sea circulation and its influence on the coastal physical oceanography outside the Pearl River Estuary, *Cont. Shelf Res.*, *24*, 1745–1760.

Sun, Z., J. Hu, Q. Zheng, and C. Li (2011), Strong near-inertial oscillations in geostrophic shear in the northern South China Sea, *J. Oceanogr.*, *67*(4), 377–384, doi:10.1007/s10872-011-0038-z.

Teague, W. J., E. Jarosz, D. W. Wang, and D. A. Mitchell (2007), Observed oceanic response over the upper continental slope and outer shelf during Hurricane Ivan*, *J. Phys. Oceanogr.*, *37*, 2181–2206.

Tian, J. W., Q. X. Yang, and W. Zhao (2009), Enhanced diapycnal mixing in the South China Sea, *J. Phys. Oceanogr.*, *39*, 3191–3203, doi:10.1175/2009jpo3899.1.

Vlasenko, V., N. Stashchuk, and K. Hutter (2005), *Baroclinic Tides: Theoretical Modeling and Observational Evidence*, Cambridge Univ. Press, Cambridge, U. K.

Wang, G., J. Su, and P. Chu (2003), Mesoscale eddies in the South China Sea observed with altimeter data, *Geophys. Res. Lett.*, *30*(21), 2121, doi:10.1029/2003GL018532.

Wang, G., J. Su, Y. Ding, and D. Chen (2007), Tropical cyclone genesis over the South China Sea, *J. Mar. Syst.*, *68*, 318–326.

Watanabe, M., and T. Hibiya (2002), Global estimates of the wind-induced energy flux to inertial motions in the surface mixed layer, *Geophys. Res. Lett.*, *29*(8), 1239, doi:10.1029/2001GL014422.

Xie, X.-H., G.-Y. Chen, X.-D. Shang, and W.-D. Fang (2008), Evolution of the semidiurnal (*M*2) internal tide on the continental slope of the northern South China Sea, *Geophys. Res. Lett.*, *35*, L13604, doi:10.1029/2008GL034179.

Xie, X.-H., X.-D. Shang, H. van Haren, G.-Y. Chen, and Y.-Z. Zhang (2011), Observations of parametric subharmonic instability-induced near-inertial waves equatorward of the critical diurnal latitude, *Geophys. Res. Lett.*, *38*, L05603, doi:10.1029/2010GL046521.

Xing, J., and A. M. Davies (2002), Processes influencing the nonlinear interaction between inertial oscillations, near-inertial internal waves, and internal tides, *Geophys. Res. Lett.*, *29*(5), 1067, doi:10.1029/2001GL014199.

Xu, Z., B. Yin, Y. Hou, and Y. Xu (2012), Variability of internal tides and near-inertial waves on the continental slope of the northwestern South China Sea, *J. Geophys. Res.*, *118*, 197–211, doi:10.1029/2012JC008212.

Zhai, X., R. J. Greatbatch, C. Eden, and T. Hibiya (2009), On the loss of wind-induced near-inertial energy to turbulent mixing in the upper ocean, *J. Phys. Oceanogr.*, *39*, 3040–3045.

Zhang, Z., W. Zhao, J. Tian, and X. Liang (2013), A mesoscale eddy pair southwest of Taiwan and its influence on deep circulation, *J. Geophys. Res. Oceans*, *118*, 6479–6494, doi:10.1002/2013JC008994.